

Global polarization of Λ hyperons in Au+Au collisions at $\sqrt{s_{\text{NN}}} = 200$ GeV

Takafumi Niida and Sergei A. Voloshin
Wayne State University

April 27, 2018

Abstract

Contents

1	Introduction	3
2	Analysis	3
2.1	Event and track selection	3
2.2	Λ reconstruction	4
2.2.1	Particle identification of daughter particles	4
2.2.2	Topological cuts	5
2.3	Event plane reconstruction	6
2.4	Polarization measurement	8
2.4.1	Invariant mass method	8
2.4.2	Event plane method	9
2.5	Effect from Feed-down	9
2.6	Systematic study	10
2.6.1	Variation of topological cuts	11
2.6.2	Method comparison: the invariant mass method and event plane method	12
2.6.3	Event plane determination	13
2.6.4	Background subtraction in Λ reconstruction	13
2.6.5	Background assumption in the invariant mass method	13
2.6.6	Uncertainty from decay parameter α	14
2.6.7	Effect of the magnetic configurations and run dependence	14
2.6.8	Cumulant correction	15
2.6.9	Acceptance correction	16
2.6.10	Effect of the tracking efficiency	20

2.6.11 Fitting range in the invariant mass method	25
3 Results	27
A Run QA for run11 and run14 Au+Au 200 GeV	32
B Calibration of the first-order event plane	34
C More plots on systematic study	36
C.1 Centrality dependence	36
C.2 p_T dependence	43
C.3 η dependence	49
C.4 A_{ch} dependence	55
D Addendum to the event plane method	61

1 Introduction

Global polarization of Λ hyperons was first measured in Au+Au collisions at $\sqrt{s_{NN}}=200$ GeV [1], where the results were consistent with zero signal just providing the upper limit. Then the polarization measurements were recently performed for the beam energy scan data ($\sqrt{s_{NN}}=7.7-39$ GeV) and non-zero signal was observed for the first time in the heavy-ion collisions [2]. The results indicate a finite thermal vorticity of the system in non-central collisions. Also, they indicate a small difference between Λ and $\bar{\Lambda}$, which would be possibly due to the effect of the magnetic field. The results are quite important for further understanding the collision dynamics and also a possible direct probe to the magnet field.

Several theoretical models [3, 4] can describe the experimental data quantitatively including the energy dependence of the global polarization, where the signal becomes smaller at higher energy. These models predict non-zero values even at $\sqrt{s_{NN}}=200$ GeV. Therefore we might be able to observe a finite signal at higher energy with a large statistics. In this note, we present results of global polarization of Λ hyperons using run10, run11, and run14 data sets of Au+Au collisions at $\sqrt{s_{NN}}=200$ GeV.

2 Analysis

2.1 Event and track selection

The minimum bias data of Au+Au collisions at $\sqrt{s_{NN}}=200$ GeV taken in 2011 was used for this analysis. Bad run rejection criteria and event selection are same as our previous analysis [5, 6]. The “period 2” which shows a relatively smaller $\langle\text{RefMult}\rangle$ compared to other periods was also removed from this analysis (run number: 12138081-12145020). Bad runs found in the study of centrality calibration was also removed from the analysis. Run QA plots are shown in Fig. 29 in Appendix. Based on this QA, outlier runs listed below are excluded from this analysis. Run and event selections are summarized below:

Run and Event selection for run10 Au+Au

- AuAu200_production, P10ik
- Trigger ID used: 260001, 260011, 260021, and 260031
- removed bad runs listed on a badrun list of StRefMultCorr and based on runQA
- $|v_z| < 30$ cm
- $|v_r| < 2$ cm from the center (vertex position in transverse plane)
- $|v_z - v_z^{\text{vpd}}| < 3$ cm
- Cut based on the correlation between RefMult and TofMult

Run and Event selection for run11 Au+Au

- AuAu200_production_2011, P11id
- Trigger ID used: 350003, 350023, 350033, and 350043
- removed bad runs listed on a badrun list of StRefMultCorr and based on runQA
- $|v_z| < 30$ cm
- $|v_r| < 2$ cm from the center (vertex position in transverse plane)
- $|v_z - v_z^{\text{vpd}}| < 3$ cm
- Cut based on the correlation between RefMult and TofMult

Run and Event selection for run14 Au+Au

- AuAu_200_production_2014, P16id
- Trigger ID used: 450050, 450060, 450005, 450015, 450025
- removed bad runs listed on a badrun list of StRefMultCorr and based on runQA
- $|v_z| < 6$ cm
- $|v_r| < 2$ cm from the center (vertex position in transverse plane)
- $|v_z - v_z^{\text{rmvpd}}| < 3$ cm
- Cut based on the correlation between RefMult and TofMult

After the event selection, global tracks were analyzed to reconstruct Λ and $\bar{\Lambda}$. The following quality cuts were applied before reconstructing Λ and $\bar{\Lambda}$:

Track selection

- $0.15 < p_T < 5$ GeV/ c
- $|\eta| < 1$
- nHitsFit ≥ 15
- nHistFit/nHitsPoss ≥ 0.52
- gDCA < 15 cm

2.2 Λ reconstruction

2.2.1 Particle identification of daughter particles

In order to reconstruct Λ particles, daughter particles of Λ , i.e. charged pions and protons, were first identified by using dE/dx information from TPC and time-of-flight

Table 1: Topological cuts for $\Lambda(\bar{\Lambda})$ reconstruction

centrality	p-DCA	π -DCA	p- π DCA	Λ DCA	decay length
10%-20%	>0.3 cm	>1.6 cm	<1.0 cm	<0.9 cm	>5.0 cm
20%-30%	>0.3 cm	>1.3 cm	<1.0 cm	<1.0 cm	>4.0 cm
30%-40%	>0.3 cm	>1.2 cm	<1.0 cm	<1.0 cm	>3.0 cm
40%-50%	>0.2 cm	>1.0 cm	<1.0 cm	<1.0 cm	>3.0 cm
50%-60%	>0.1 cm	>0.9 cm	<1.0 cm	<1.0 cm	>3.0 cm

information from TOF. The cuts to select the daughter particles were summarized below:

charged pions:

- $|n\sigma_{\pi}^{TPC}| < 3$
- $0.017 - 0.013 \times p < m^2 < 0.04$ [GeV/c]

protons and antiprotons:

- $|n\sigma_p^{TPC}| < 3$
- $0.5 < m^2 < 1.5$ [GeV/c]

If tracks do not have TOF information, the mass square (m^2) cuts were not required.

2.2.2 Topological cuts

The following topological cuts were applied to increase the signal to background ratio.

- proton DCA from the primary vertex
- pion DCA from the primary vertex
- DCA between two daughter tracks
- decay length
- DCA of $\Lambda(\bar{\Lambda})$ from the primary vertex
- moving direction of $\Lambda(\bar{\Lambda})$ is to be away from the primary vertex

The decay length is a distance from the primary vertex to the $\Lambda(\bar{\Lambda})$ decay vertex. These cuts are determined so that the background level is at least below 30% in more central collisions. Final cuts used in this analysis are summarized in Table 1. Figure 1 shows the invariant mass distributions of $p\pi^-$ pairs for Λ and $\bar{p}\pi^+$ pairs applying the topological cuts step-by-step. As seen in the figure, the daughter DCA cuts significantly reduce the background and other cuts work for further improvement of the signal to background ratio.

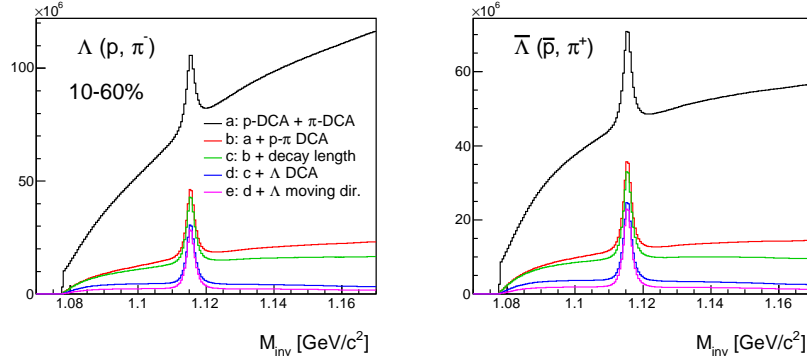


Fig. 1: Invariant mass distributions of $p\pi^-$ pair candidates for Λ and $\bar{p}\pi^+$ pair candidates for $\bar{\Lambda}$ for 10-60% centrality in Au+Au collisions at $\sqrt{s_{NN}} = 200$ GeV, when applying the topological cuts step-by-step.

2.3 Event plane reconstruction

Λ Polarization can be measured by looking at the correlation between azimuthal angle of daughter proton in the Λ rest frame and the reaction plane (see the following section for the detail). We used the first-order event plane as the reaction plane, which determined by the spectator neutrons measured in ZDCSMDs. The detail of the event plane calibration can be found in Ref. [5] and Appendix B. Figure 2 shows the resolution of Ψ_1 for ZDCSMD east or west or combined plane in Au+Au collisions at $\sqrt{s_{NN}} = 200$ GeV for run10, run11, and run14 data. The resolution was estimated in the way proposed by Ref. [7]. The resolution for run14 is 5% larger than that for run10 and run11.

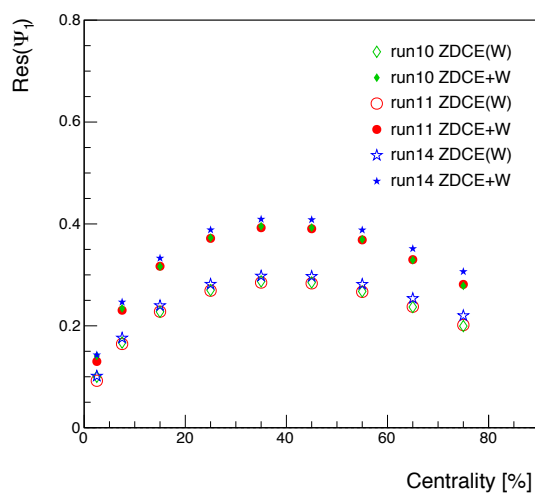


Fig. 2: Resolution of the first-order event planes for ZDCSMDs in run10, run11, and run14. ZDCE+W denotes the combined plane of ZDC east and west.

2.4 Polarization measurement

The direction of the initial angular momentum of the system, \mathbf{L} , in non-central collisions is perpendicular to the direction of the reaction plane. Furthermore since hyperons do parity-violating decay, the daughter baryon is preferentially emitted to the direction of the hyperon spin (if the parent particle is anti-particle, the daughter baryon tends to be emitted to opposite direction of the parent spin.). Therefore the global polarization of Λ hyperons can be measured with [1]:

$$P_H = \frac{8}{\pi\alpha_H} \langle \sin(\Psi_{\text{RP}} - \phi_p^*) \rangle, \quad (1)$$

where α_H is the hyperon decay parameter ($\alpha_\Lambda = -\alpha_{\bar{\Lambda}} = 0.642 \pm 0.013$) and ϕ_p^* denotes the azimuthal angle of the daughter proton in the Λ rest frame. Similar to the directed flow measurement, the first-order event plane Ψ_1 was used as the reaction plane. Thus in order to take into account the experimental resolution of the event plane Eq. 1 can be written as:

$$P_H = \frac{8}{\pi\alpha_H} \frac{\langle \sin(\Psi_1 - \phi_p^*) \rangle}{\text{Res}(\Psi_1)}, \quad (2)$$

where $\text{Res}(\Psi_1)$ is the event plane resolution shown in Fig. 2.

2.4.1 Invariant mass method

The invariant mass method, which is commonly used in the flow analysis, was used to extract the polarization signal. Figure 3 shows $\langle \sin(\Psi_1 - \phi_p^*) \rangle$ as a function of the invariant mass of (p, π^-) pairs. Around the Λ mass region ($M_{\text{inv}} \sim 1.11568 \text{ GeV}/c^2$), non-zero signals can be seen systematically. Note that the polarization signal for $\bar{\Lambda}$ has an opposite sign to that for Λ because the daughter baryon is preferentially emitted to the opposite direction of its parent spin. To extract that signal, the data was fitted with the following equation:

$$\langle \sin(\Delta\phi) \rangle^{\text{obs}} = (1 - f^{\text{Bg}}(M_{\text{inv}})) \langle \sin(\Delta\phi) \rangle^{\text{Sg}} + f^{\text{Bg}}(M_{\text{inv}}) \langle \sin(\Delta\phi) \rangle^{\text{Bg}} \quad (3)$$

where f^{Bg} is a background fraction as a function of the invariant mass and $\Delta\phi = \Psi_1 - \phi_p^*$. The $\langle \sin(\Delta\phi) \rangle^{\text{Sg}}$ is the polarization signal of $\Lambda(\bar{\Lambda})$ and the $\langle \sin(\Delta\phi) \rangle^{\text{Bg}}$ is a background contribution which is supposed to be zero but could be non-zero value, for example due to mis-identification of protons as pions. Since the shape of the background signal with the invariant mass is unknown, a linear function ($\langle \sin(\Delta\phi) \rangle^{\text{Bg}} = \alpha + \beta M_{\text{inv}}$) was assumed for that as shown with red lines in Fig. 3. We also fitted the data assuming that the background signal is zero ($\alpha = 0$ and $\beta = 0$) as shown with blue lines in Fig. 3. The signals obtained in each case were consistent within the statistical uncertainties. We will discuss this in the section of the systematic uncertainty.

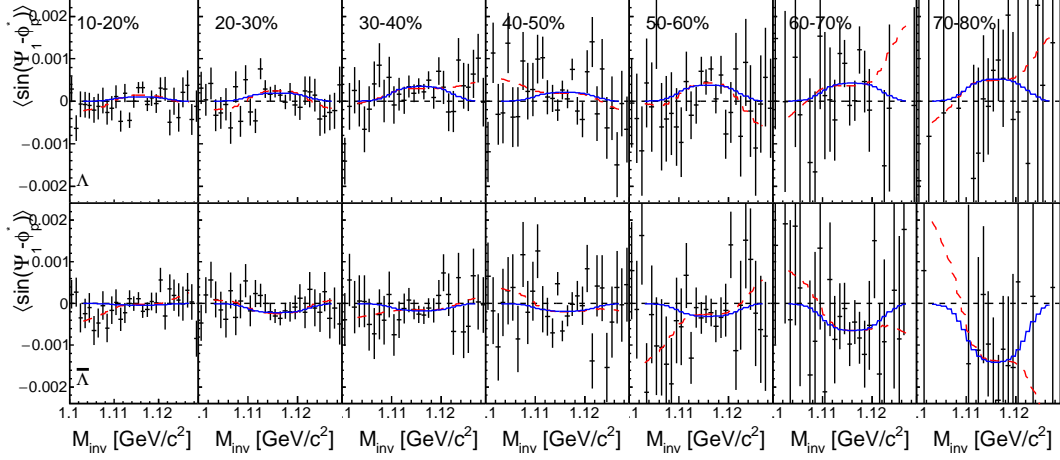


Fig. 3: $\langle \sin(\Delta\phi) \rangle$ as a function of the invariant mass of $(p\pi^-)$ and $(\bar{p}\pi^+)$ pairs for Λ and $\bar{\Lambda}$ for each centrality bin. Solid lines show the fitting function defined with Eq. 3 for two different background assumptions (see text for the detail).

2.4.2 Event plane method

One can also subtract the signal by counting the number of $\Lambda(\bar{\Lambda})$ in each azimuthal bin of $\Psi_1 - \phi_p^*$ and fitting it with a sine function like the flow analysis (here we call this method as “event plane method”). Figure 4 shows the invariant mass distribution of $(p\pi^-)$ and $(\bar{p}\pi^+)$ pairs for 30%-40% centrality in a bin of $-1 < (\Psi_1 - \phi_p^*)/\pi < -2/3$ for real events and mixed events with similar centrality, z-vertex, and second-order event plane. The background distribution is described well by the mixed events. Then the number of Λ or $\bar{\Lambda}$ was counted within the mass range of $1.1105 < M_{\text{inv}} < 1.121$ after subtracting the normalized mass distribution of mixed events from the distribution of real events. Figure 5 shows the number of Λ and $\bar{\Lambda}$ as a function of $\Psi_1 - \phi_p^*$ after the background subtraction. Then the data was fitted with the following function, $p_0(1 + 2p_1 \sin(\Psi_1 - \phi_p^*))$, to extract the signal. As you can see, the data have a cosine term and is not well described only with the sine term. However even if we include cosine terms including higher-orders, we confirmed that the extracted sine term does not change so much. The cosine component in the data can be explained by the elliptic flow. Please see Appendix [?] for more detailed study.

2.5 Effect from Feed-down

A sizable amount of Λ and $\bar{\Lambda}$ produced in the collisions are secondary particles decaying from heavier particles such as $\Sigma^* \rightarrow \Lambda + \pi$, $\Sigma^0 \rightarrow \Lambda \gamma$, and $\Xi \rightarrow \Lambda \pi$. The parent particles would be also polarized and then the polarization is transferred from the parent particle

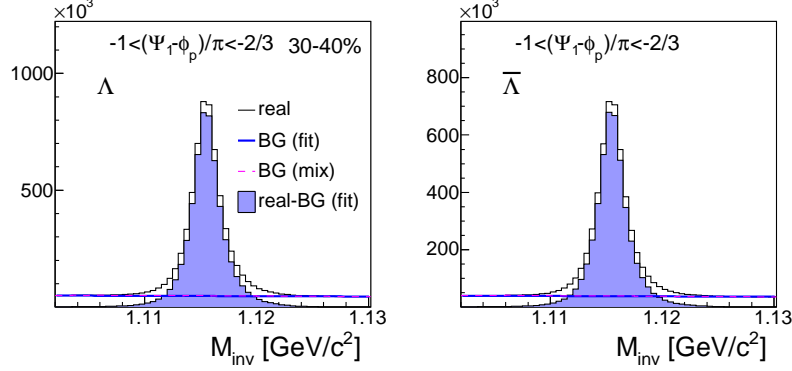


Fig. 4: The invariant mass of $(p\pi^-)$ and $(\bar{p}\pi^+)$ pairs for Λ and $\bar{\Lambda}$ for 30%-40% centrality. Black solid lines show the distribution from real events, magenta dashed lines show that from mixed events, and blue bold lines show the linear fitting function to the background. Filled area shows the distribution after subtracting the background distribution from the fitting.

to daughter Λ . The contribution of such feed-downs to the measured polarization was studied and estimated in Ref. [8, 3, 4] and is found to dilute the polarization by 15%–20%. Note that this estimate is model-dependent and in addition it might be lower in the experimental results due to a reduction of secondary particles by a requirement of topological cuts. Therefore we compare our results to the model calculations which does and does not take into account the feed-down effect, instead of correcting the data.

2.6 Systematic study

The following sources were considered to estimate systematic uncertainties:

- Variation of topological cuts
- Method comparison: the invariant mass method and event plane method
- Event plane determination
- Background subtraction in Λ reconstruction
- Background assumption in the invariant mass method
- Uncertainty from the decay parameter α

The details of these studies can be found in the following sub-sections and Appendix. Systematic uncertainties were calculated by the square root of quadratic sum of uncertainties from each source. However we found that the estimated uncertainties were dominated by statistical fluctuations. Since the difference between the default result and

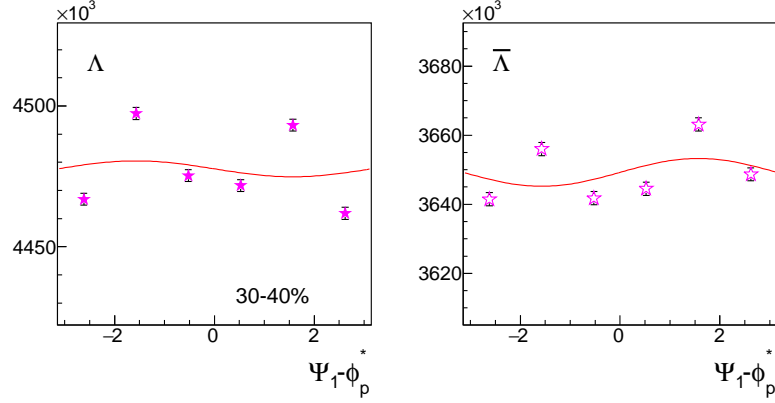


Fig. 5: Extracted number of Λ and $\bar{\Lambda}$ as a function of $\Psi_1 - \phi_p^*$ for 30%-40% centrality. The data was fitted with sine function as shown with solid lines (see text for the detail).

each systematic source did not show any significant centrality or p_T or η dependence and each data point are in agreement with the default values within the statistical uncertainties, we fitted the difference with a constant function and assigned it as the systematic uncertainty of that source. To be more conservative, we added “the error of error” to that estimated constant values. The details can be found in Appendix and our presentation in:

http://www.star.bnl.gov/protected/bulkcorr/taknn/2017/1220_pol_afterPWGC_revised.pdf

Furthermore, the following systematic studies were performed to confirm that the observed signal were not affected by any experimental bias:

- Effect of the magnetic configuration and run dependence
- Cumulant correction to see the effect of non-uniform acceptance in azimuth
- Acceptance correction for rapidity angle
- Effect of the tracking efficiency
- Fitting range in the invariant mass method

These studies are also summarized in the following sub-sections but they are not included in final systematic uncertainties.

2.6.1 Variation of topological cuts

As described in Sec. 2.2.2 and summarized in Table 1, the topological cuts were applied to reduce the combinatorial background when reconstructing Λ and $\bar{\Lambda}$. Those topological cuts were varied to looser or tighter ones to estimate the systematic uncertainties.

For example, the dca of daughter particles and $\Lambda(\bar{\Lambda})$ to the primary vertex and the dca between two daughters were varied by ± 0.1 cm, and the decay length was varied by ± 1 cm, which correspond to 10-30% variation from the default cut. Note that these are larger variation than the previous publication on multi-strangeness elliptic flow [13]. Figure 6 shows Λ polarization as a function of centrality when varying one of the topological cuts. Results do not change significantly and the systematic uncertainty from the topological cuts was determined as the standard deviation of these results and estimated as $< 3\%$.

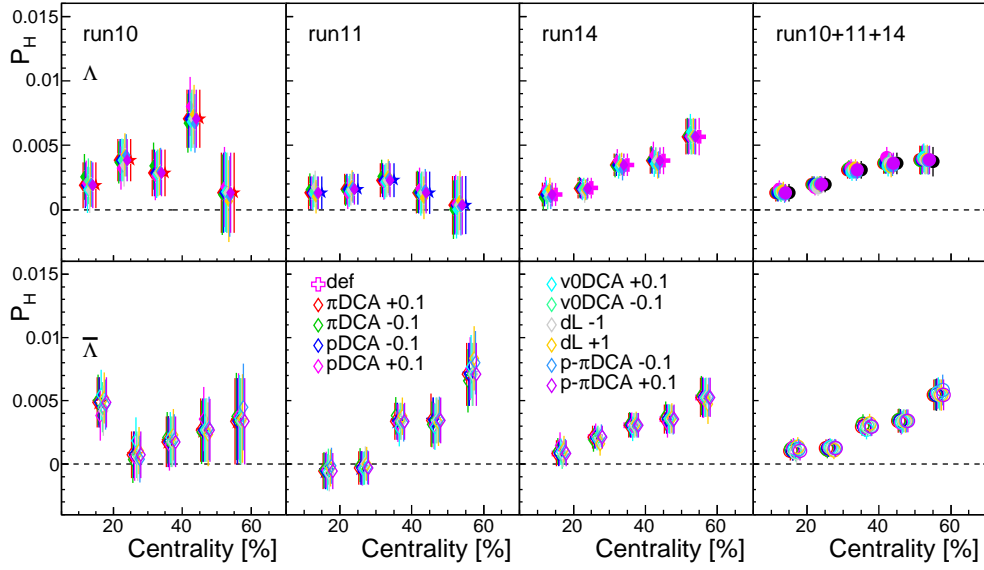


Fig. 6: Global polarization of Λ and $\bar{\Lambda}$ as a function of centrality for different topological cuts.

2.6.2 Method comparison: the invariant mass method and event plane method

As explained in the previous section, two methods, i.e. the invariant mass method and event plane method, were used to extract the polarization signal. Figure 8 shows Λ polarization vs centrality measured with those two methods. The results from the event plane method are in good agreement with the results from the invariant method within their statistical uncertainties. The difference between the mean data points was considered in the systematic uncertainty.

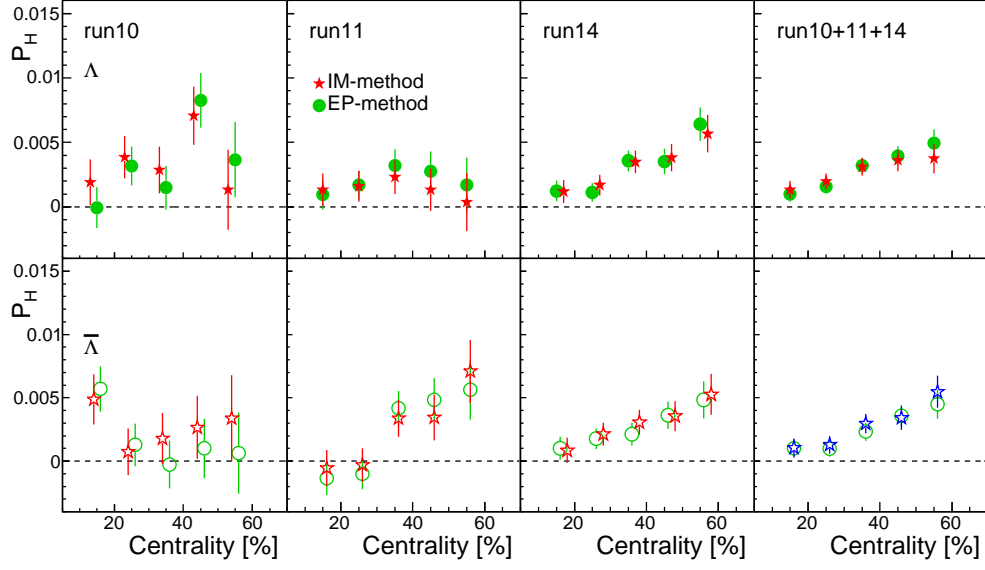


Fig. 7: Global polarization of Λ and $\bar{\Lambda}$ as a function of centrality measured with the invariant method and the event plane method.

2.6.3 Event plane determination

In the default calculation, the first-order event plane was determined by both ZDC-SMDs in the east and west sides. As a systematic check, we used one of them as the event plane, although the resolution becomes worse as shown in Fig. 2.

2.6.4 Background subtraction in Λ reconstruction

To obtain the polarization signal with the invariant mass method, the signal to background ratio for (anti-) Λ samples is needed. In the default calculation, the linear function was used to fit the combinatorial background and extract the signal and background. We also tested the event mixing technique to subtract the background as shown in Fig. 4. Figure 9 shows the comparison between results from the fitting and event-mixing methods used to estimate the background level. The difference was taken into account in the systematic uncertainties, although the effect is quite small.

2.6.5 Background assumption in the invariant mass method

As shown in Fig. 4, a level of the combinatorial background within Λ mass peak is about 10%-20% for run10 and run11, and it becomes slightly larger for run14 up to 30% in more central collisions. This background is supposed to not have any polarization signal. We assumed that the background has no polarization as a default condition

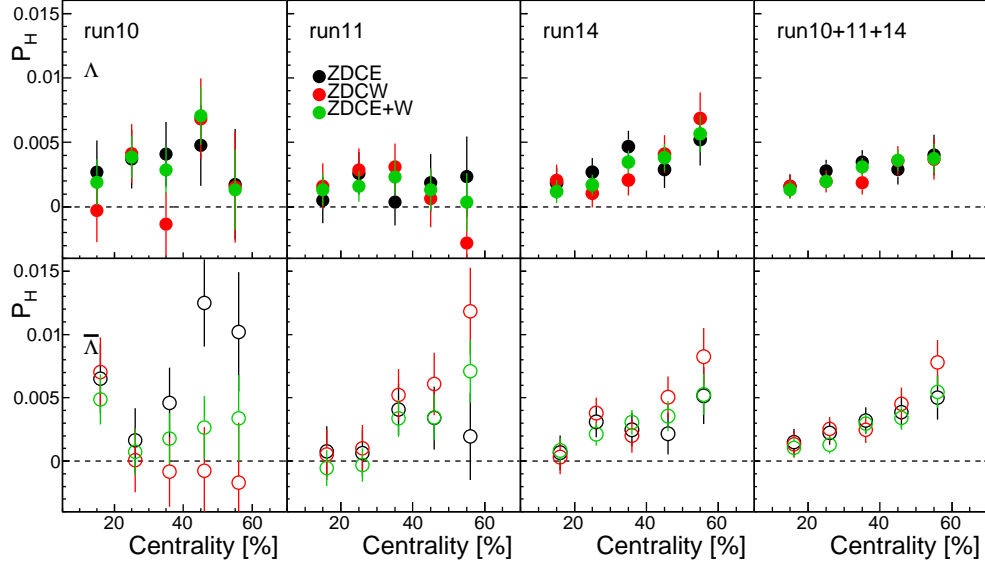


Fig. 8: Global polarization of Λ and $\bar{\Lambda}$ as a function of centrality measured with ZDCSMD east, west, and combined planes.

and used the fit function Eq. 3 with $\alpha = \beta = 0$. As explained in Sec. 2.4.1, we also tested non-zero background fit function. Results using two fit functions are shown in Fig. 10. Even if we assume non-zero background contribution, the results are in good agreement with the case of zero-background assumption.

We also checked if there is a signal in off-mass-peak region when increasing the background by making topological cuts looser. Figure 11 shows the invariant mass distributions and $\langle \sin(\Psi_1 - \phi_p^*) \rangle$ of Λ for different centrality bins. As seen in the figure, the background contribution is likely very small.

2.6.6 Uncertainty from decay parameter α

According to Ref. [12], the decay parameter of $\Lambda \rightarrow p\pi^-$, α^- , is 0.642 ± 0.013 , while $\alpha_+ = 0.71 \pm 0.08$ for $\bar{\Lambda} \rightarrow \bar{p}\pi^+$. If CP is conserved, $\alpha_- = -\alpha_+$. In this study, we take $\alpha_- = -\alpha_+ = 0.642 \pm 0.013$ and the uncertainty of α_{\pm} was incorporated in the systematic uncertainty (2%). Also the difference from the case using $\alpha_+ = 0.71$ was taken into account in the systematic uncertainty. This effect is 9.6% for $\bar{\Lambda}$.

2.6.7 Effect of the magnetic configurations and run dependence

In order to investigate a possible effect from the polarity of the magnetic field on the observed signal of polarization, we divided the run11 data to two groups; Reverse Full

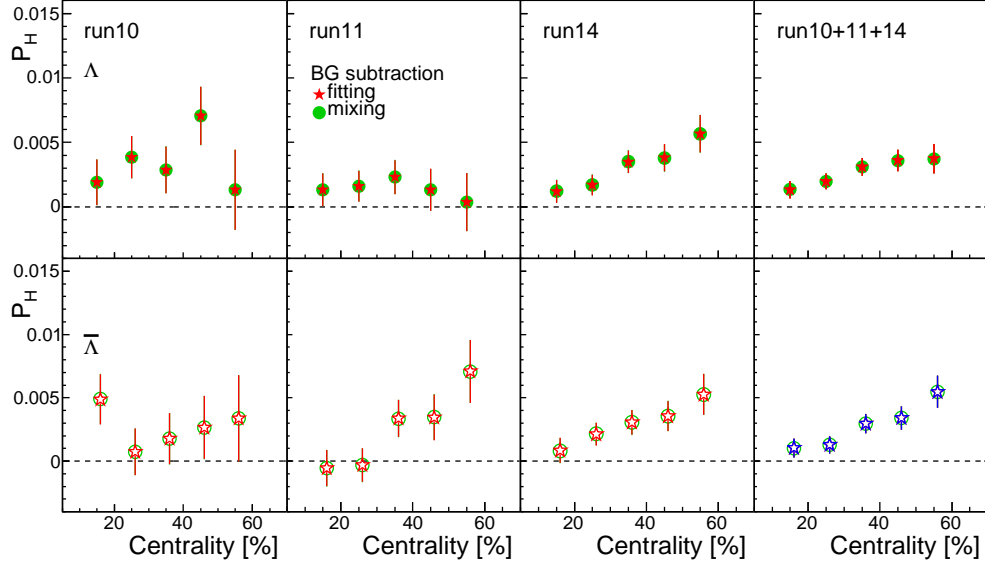


Fig. 9: Global polarization of Λ and $\bar{\Lambda}$ as a function of centrality for two different background subtraction methods.

Field runs (RF, run number: 12126104-12152016) and Full Field runs (FF, run number: 12153008-12171016). Figure 12 shows P_H as a function of centrality for RF and FF runs. We confirmed that there is no significant difference between both runs beyond the uncertainties. This study also indicates that there is no significant run dependence. Note that in run11 the trigger condition changed several times with runs.

2.6.8 Cumulant correction

In order to check the effect of non-uniform acceptance in azimuth, the cumulant correction was performed. The correction terms were subtracted from the observed signal as follows:

$$\langle\langle\sin(\Psi_1 - \phi_p^*)\rangle\rangle - \langle\langle\sin(\Psi_1)\rangle\rangle\langle\langle\cos(\phi_p^*)\rangle\rangle + \langle\langle\cos(\Psi_1)\rangle\rangle\langle\langle\sin(\phi_p^*)\rangle\rangle \quad (4)$$

where the double brackets indicate an average over particles first and then an average over events. Figure 13 shows the observed $\langle\langle\sin(\Psi_1 - \phi_p^*)\rangle\rangle$ of $\bar{\Lambda}$ and the corresponding correction terms in Eq. 4. In the middle row, the mean sine and cosine of daughter proton azimuthal angle in $\bar{\Lambda}$ rest frame, $\langle\langle\sin(\phi_p^*)\rangle\rangle$ and $\langle\langle\cos(\phi_p^*)\rangle\rangle$. They show some structures near $\bar{\Lambda}$ mass peak. In the bottom row, the mean sine and cosine of the event plane, $\langle\langle\sin(\Psi_1)\rangle\rangle$ and $\langle\langle\cos(\Psi_1)\rangle\rangle$, are shown and have no specific structure. Then the correction terms are shown in the first row together with the observed signal. It is found that the correction terms are very small compared to the observed signal,

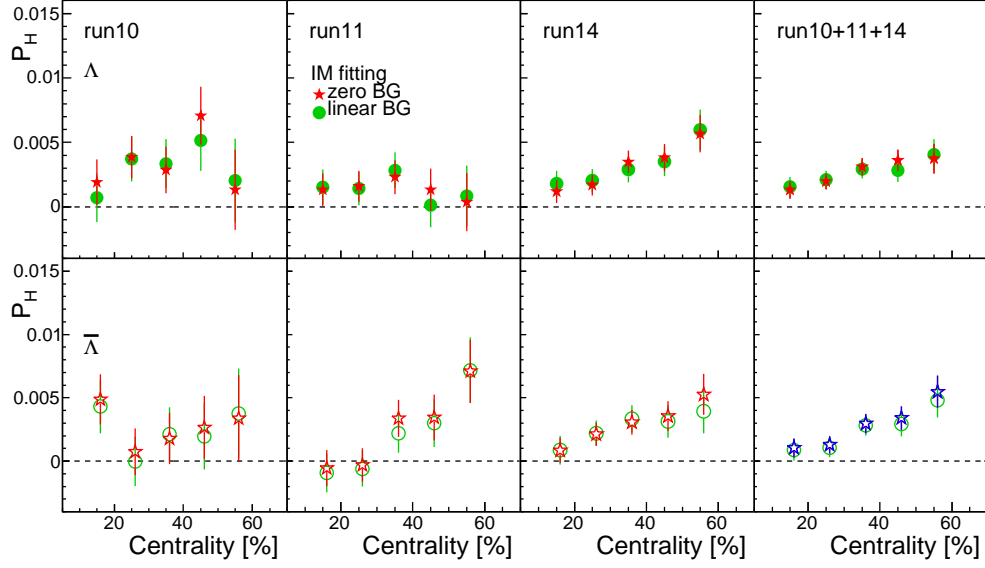


Fig. 10: Global polarization of Λ and $\bar{\Lambda}$ as a function of centrality using the fit functions with zero and non-zero background assumptions in the invariant mass method.

especially around the $\bar{\Lambda}$ mass. The polarization signal was extracted after subtracting the correction terms in the same way as explained in previous section as shown in Fig. 14. The results with the correction are in good agreement with the results without the correction. Therefore we did not apply this correction in the final results.

2.6.9 Acceptance correction

Acceptance correction was studied in the previous STAR paper [1], in this case including the effect from the limited acceptance in longitudinal direction. The measured polarization can be written as:

$$\frac{8}{\pi\alpha_H}\langle\sin(\Psi_{RP})\rangle = A_0(p_T^H, \eta_H^H)P_H(p_T^H, \eta^H) - A_2(p_T^H, \eta_H^H)P_H^{(2)}(p_T^H, \eta^H) \quad (5)$$

where A_0 and A_2 are the acceptance correction functions and are defined as follows:

$$A_0(p_T^H, \eta_T^H) = \frac{4}{\pi}\langle\sin(\theta^*)\rangle \quad (6)$$

$$A_2(p_T^H, \eta_T^H) = \frac{2}{\pi}\langle\sin(\theta^*)\cos[2(\phi_H - \phi_p^*)]\rangle. \quad (7)$$

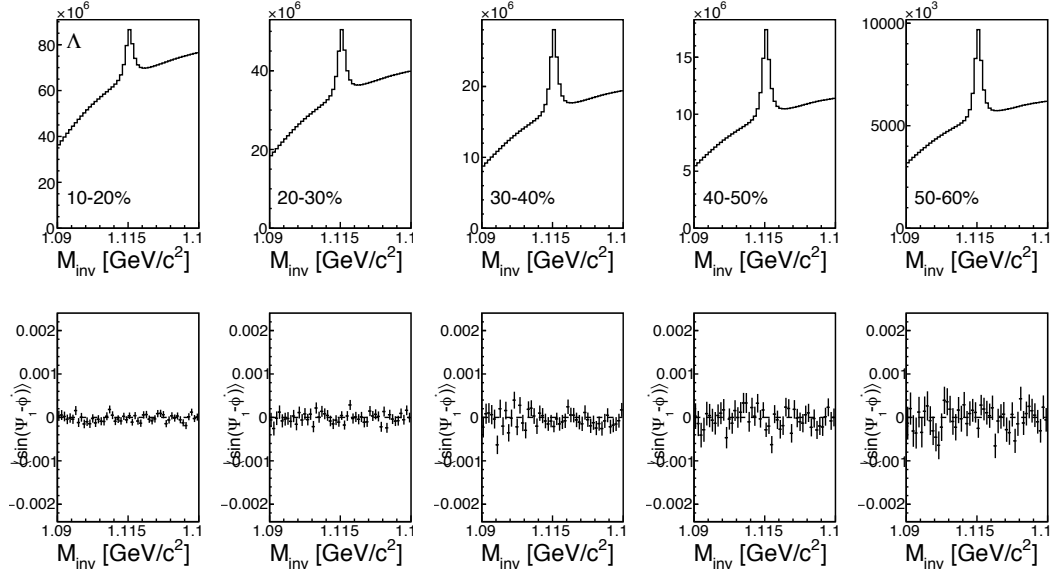


Fig. 11: Invariant mass (M_{inv}) distributions for Λ and $\langle \sin(\Psi_1 - \phi_p^*) \rangle$ as a function of M_{inv} for different centrality bins with loose topological cuts.

The $P_H^{(2n)}$ is a true signal of the polarization in the form of the Fourier expansion considering its azimuthal angle dependence.

$$P_H = \sum_{n=0} P_H^{(2n)} \cos[2n(\phi_H - \Psi_{RP})], \quad (8)$$

where the sum is performed over even harmonics due to the symmetry of the system. The correction factor was calculated based on the experimental data from Eq. 6 and Eq. 7. Since we do not measure $P_H^{(2)}$, only the first term in Eq. 5 was considered and applied to the final results.

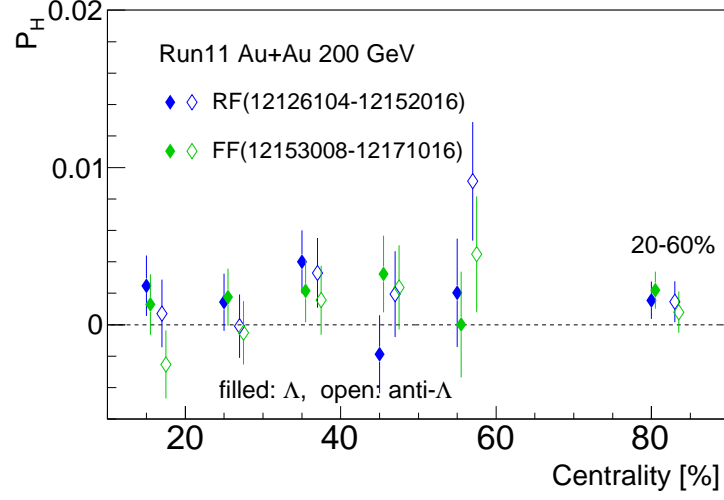


Fig. 12: Global polarization of Λ and $\bar{\Lambda}$ as a function of centrality for runs with two different magnetic configurations.

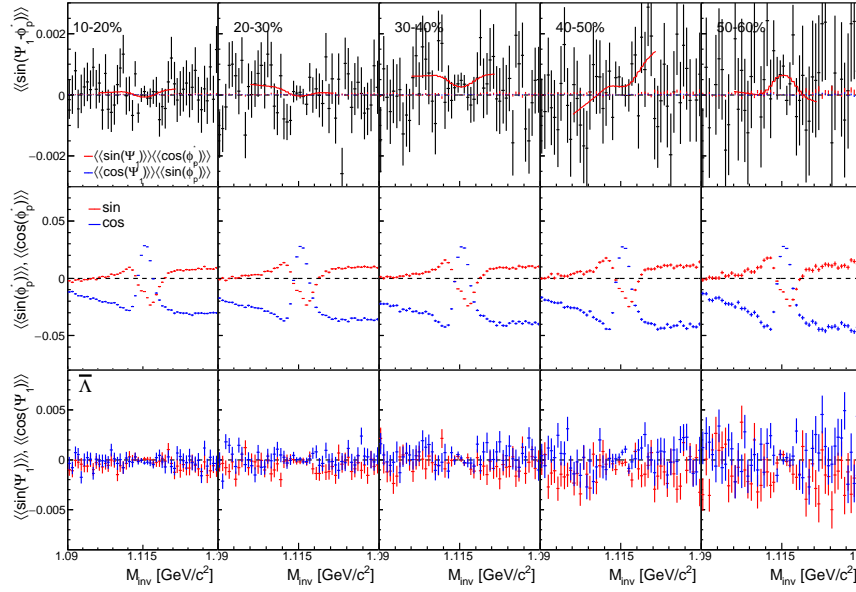


Fig. 13: (Top) $\langle\langle\sin(\Psi_1 - \phi_p^*)\rangle\rangle$ with the first and second cumulant correction terms in Eq. 4, (Middle) average sine and cosine of ϕ_p^* , and (Bottom) average sine and cosine of Ψ_1 determined by ZDCSMD east and west, as a function of the invariant mass for $\bar{\Lambda}$ in different centrality bins.

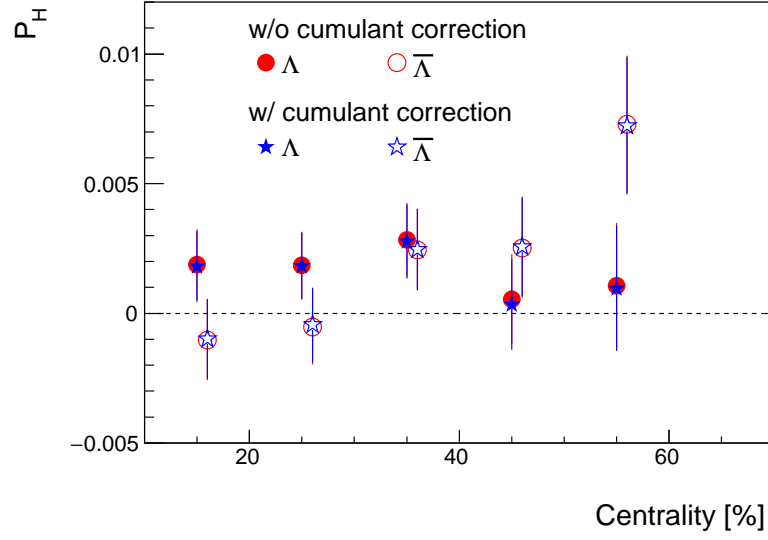


Fig. 14: Global polarization with and without the cumulant correction with run11 data.

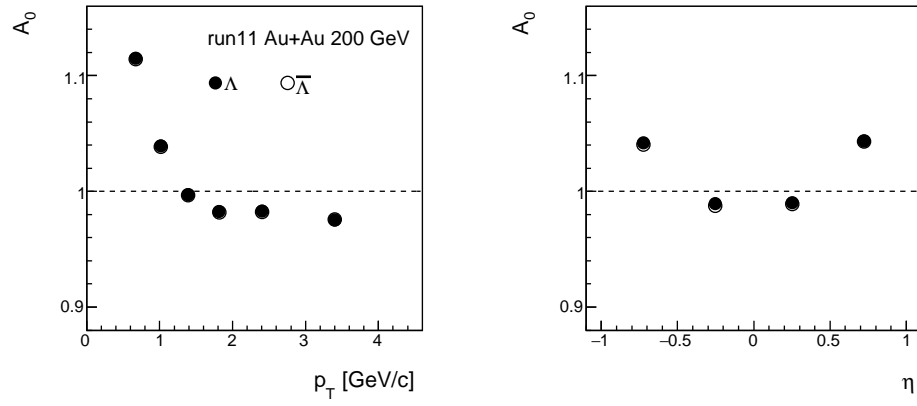


Fig. 15: Acceptance correction factors depending on p_T and η of Λ and $\bar{\Lambda}$ in Au+Au collisions at $\sqrt{s_{NN}} = 200$ GeV for run11 data set.

2.6.10 Effect of the tracking efficiency

The effect of track efficiency to the final results was studied. Figure 16 shows tracking efficiency of Λ and $\bar{\Lambda}$ for run11 obtained by using the embedding data. The data were fitted with the following function, $p_0 * \exp(-(p_1/p_T)^{p_2})$, where p_i is free parameters.

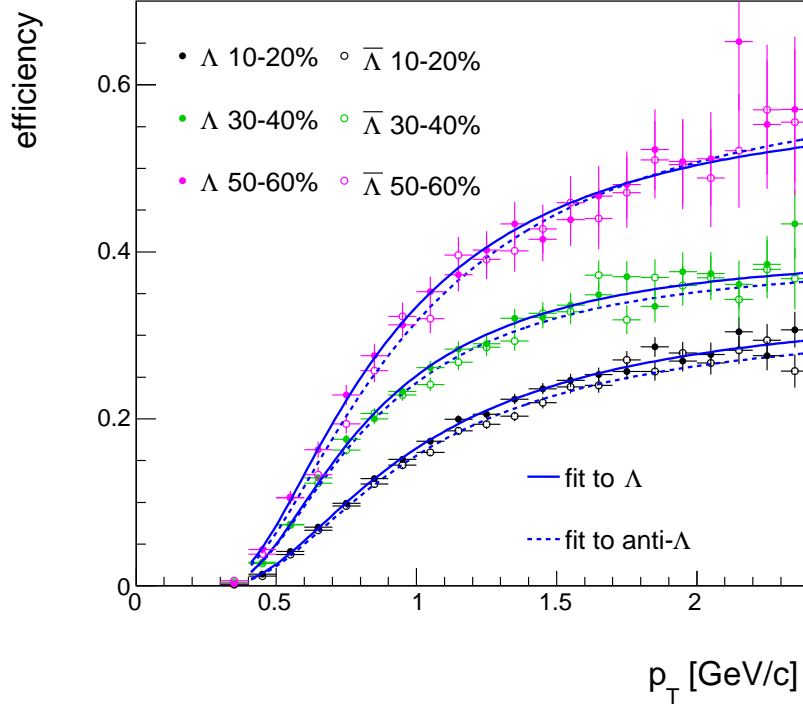


Fig. 16: Tracking efficiency of Λ and $\bar{\Lambda}$ in Au+Au collisions at $\sqrt{s_{NN}} = 200$ GeV for run11 data set.

For run14 data, the relative efficiency to run11 was estimated by using real data. Top panels in Fig. 17 and Fig. 18 show raw yields of Λ and $\bar{\Lambda}$ as a function of p_T for different centrality bins in run11 and run14. Bottom panels show the ratio of run11 to run14 data. The ratio was found to drop at lower p_T and also showed smaller values in more central events. It could be due to HFT included in run14. For run14 data, this relative efficiency in addition to the tracking efficiency from run11 data was applied for the correction. For the correction, these efficiencies normalized relative to those in peripheral events were used.

Figure 19 and 20 show the similar plot but for run11 and run10 data. The ratio of run10 to run10 data is almost constant over p_T , therefore the normalized tracking efficiency for run11 was used for the correction on run10 data.

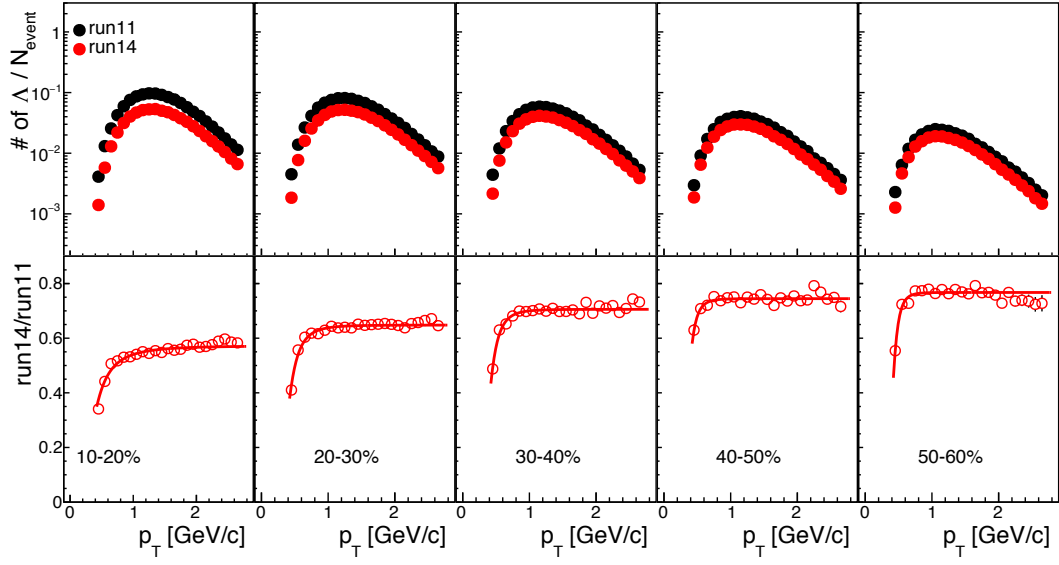


Fig. 17: Raw p_T distribution and the relative efficiency of Λ in run11 to that in run14.

Figure 21 shows global polarization of Λ and $\bar{\Lambda}$ as a function of centrality with and without the efficiency correction for run14. It was found that the efficiency correction didn't change the results beyond the statistical uncertainties, as expected from no significant p_T dependence of the polarization. Therefore we didn't apply the efficiency correction to the final results.

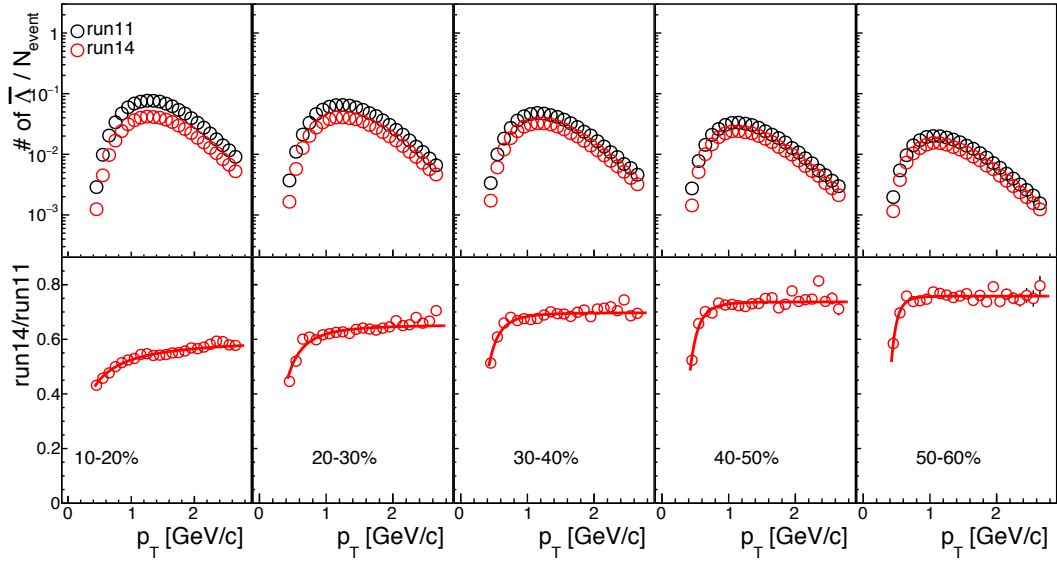


Fig. 18: Raw p_T distribution and the relative efficiency of $\bar{\Lambda}$ in run11 to that in run14.

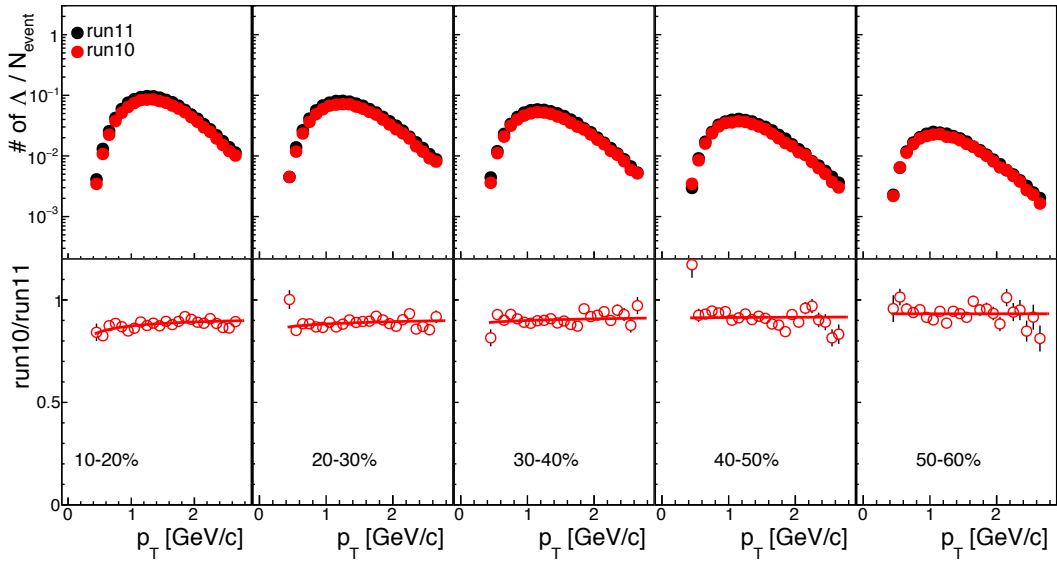


Fig. 19: Raw p_T distribution and the relative efficiency of Λ in run11 to that in run10.

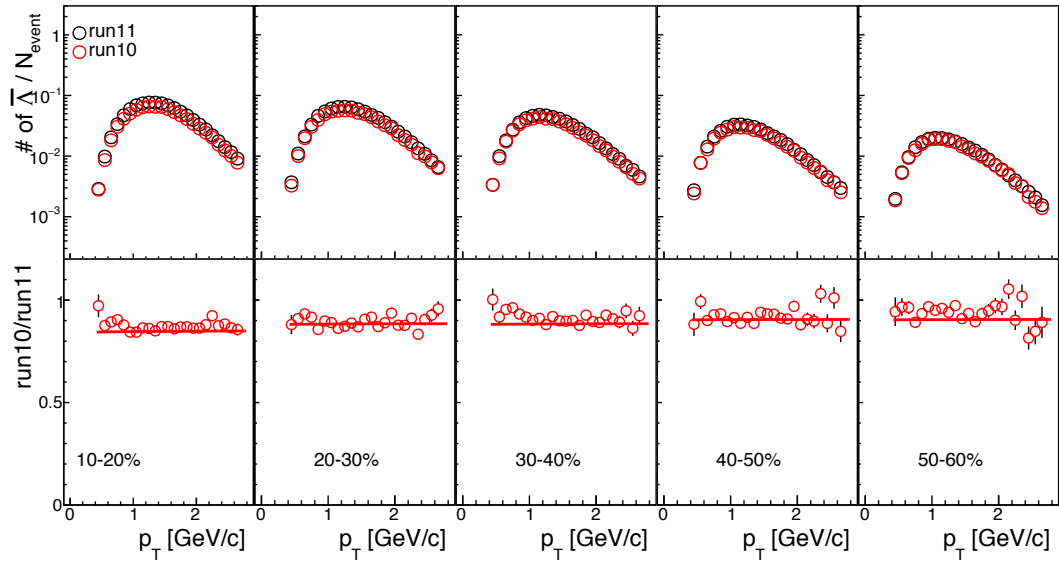


Fig. 20: Raw p_T distribution and the relative efficiency of $\bar{\Lambda}$ in run11 to that in run10.

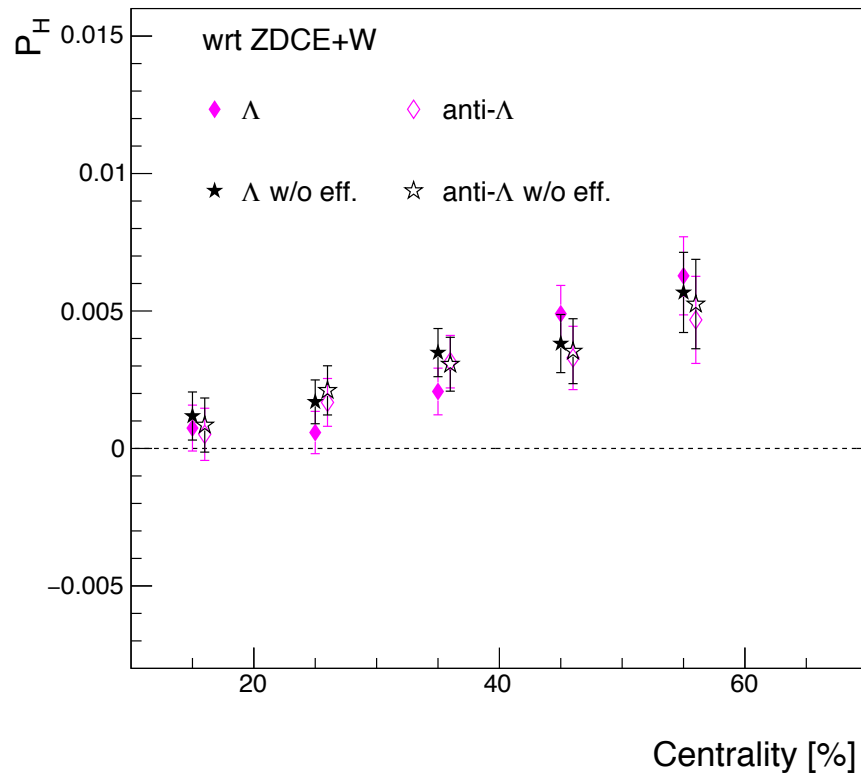


Fig. 21: Global polarization of Λ and $\bar{\Lambda}$ with and without the efficiency correction in run14.

2.6.11 Fitting range in the invariant mass method

In the invariant mass method, the fitting was performed in the mass range of $1.103 < M_{inv} < 1.127$. To check the effect of the fitting range, a wider range of $1.1 < M_{inv} < 1.13$ was tested as shown in Fig. 22. Figure 23 shows global polarization for results with two different fitting ranges. We found that results from the wider fitting range was very consistent with results from the default fitting range. Since this effect is negligible, we didn't include it to the systematic uncertainties.

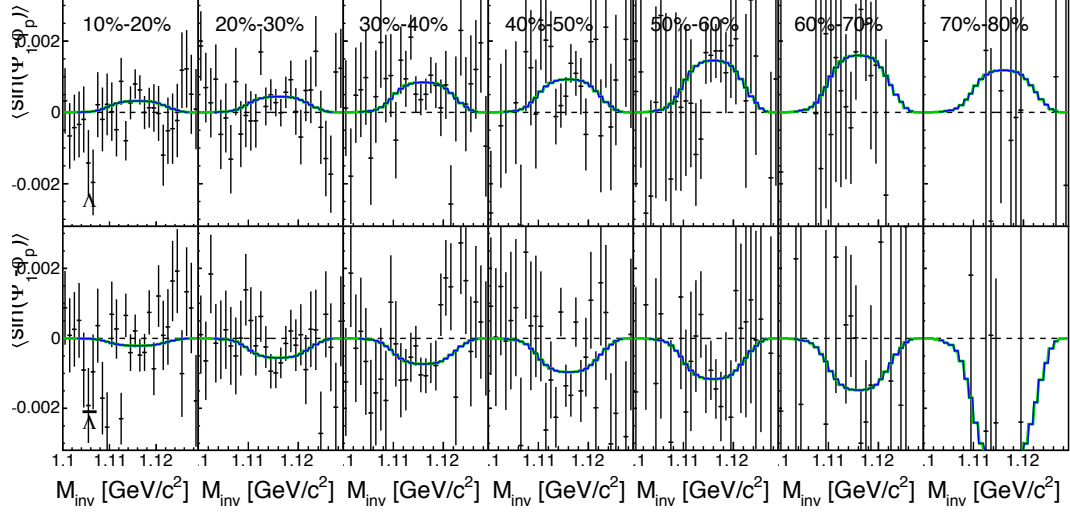


Fig. 22: Mean sine of $\Psi_1 - \phi_p^*$ as a function of M_{inv} for Λ and $\bar{\Lambda}$ in run14, where the event plane resolution was corrected. Two fitting ranges were shown.

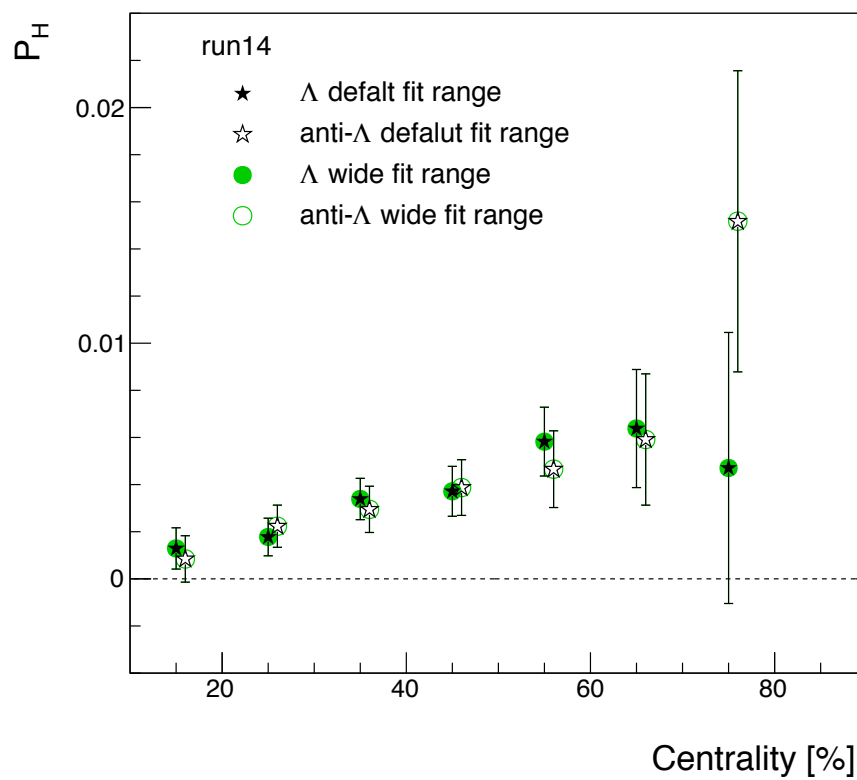


Fig. 23: Global polarization of Λ and $\bar{\Lambda}$ as a function of centrality in run14 for two different fitting ranges in the invariant mass method.

3 Results

Figure 24 shows the collision energy dependence of average polarization for Λ and $\bar{\Lambda}$. The data from previous STAR publications are shown together [1, 2]. By a significant improvement of the statistics compared to run4 data used in Ref. [1], finite signals are observed for Λ and $\bar{\Lambda}$ and follow a global trend of the collision energy dependence. No significant difference between Λ and $\bar{\Lambda}$ was observed at $\sqrt{s_{NN}} = 200$ GeV. Calculations from hydrodynamic model [3] and a multi-phase transport model (AMPT) [4] are compared to the data. Solid lines are for primary Λ and dashed lines are for Λ including the effect of feed-down. These models qualitatively agree to the data with the global trend of the energy dependence.

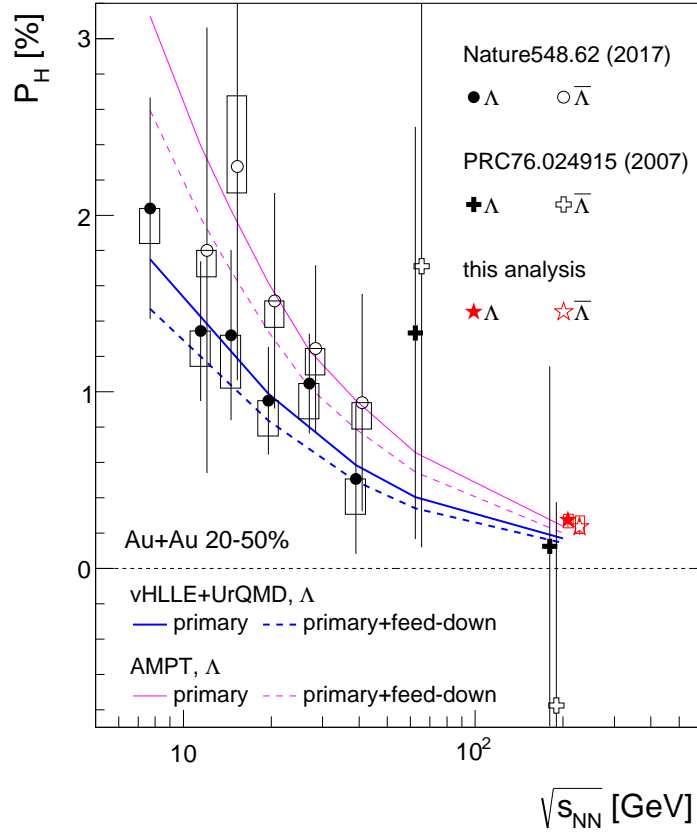


Fig. 24: Polarization of Λ and $\bar{\Lambda}$ as a function of the collisions beam energy in Au+Au collisions, comparing to the hydrodynamic model and AMPT calculations. Solid lines show the calculations only for primary Λ and dashed lines includes Λ from a feed-down.

Figure 25 shows centrality dependence of the polarization in Au+Au collisions at $\sqrt{s_{NN}} = 200$ GeV. The polarization systematically becomes larger in more peripheral collisions, which is consistent with an expectation of larger thermal vorticity in more peripheral collisions [10], although the uncertainties are still large.

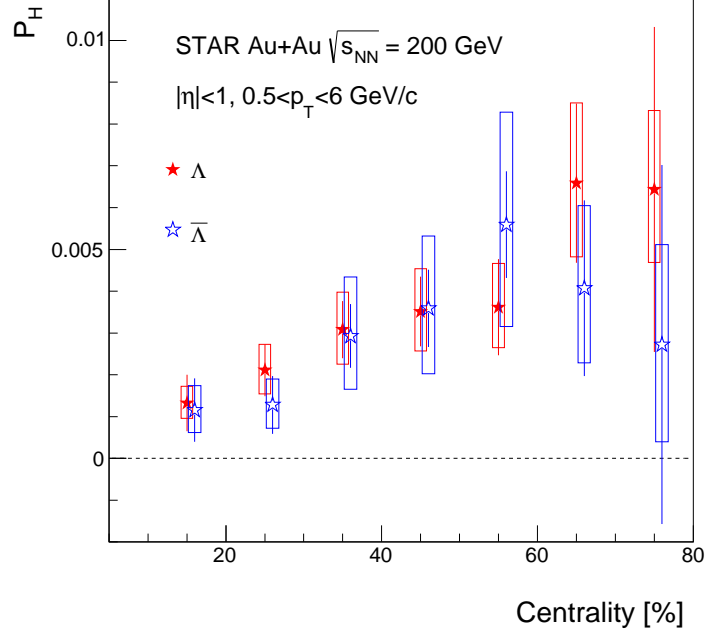


Fig. 25: Polarization of Λ and $\bar{\Lambda}$ as a function of centrality in Au+Au collisions at $\sqrt{s_{NN}} = 200$ GeV.

Figure 26 shows p_T dependence of the polarization, comparing with hydrodynamic model calculations with two different initial conditions; UrQMD initial condition and Galuber with the initial source tilt [11]. Results do not show any strong p_T dependence beyond the uncertainties. The model calculations slightly underestimate the values but show a very weak p_T dependence similar to the data. The data seems to be closer to the UrQMD initial condition.

Figure 27 shows η dependence of the polarization in 20%-60% centrality bin. As expected from the baryon transparency and our TPC acceptance, the data do not show any η dependence.

We have studied an average polarization due to a thermal vorticity of the system. There might be an additional contribution to the polarization, which is closely related to the Chiral phenomena. If there is Charge Separation Effect [14], an axial current J_5 would be generated along the direction of the initial magnetic field ($J_5 \propto \mu_v \vec{B}$) which is also perpendicular to the reaction plane. Spin of particles in the axial current are

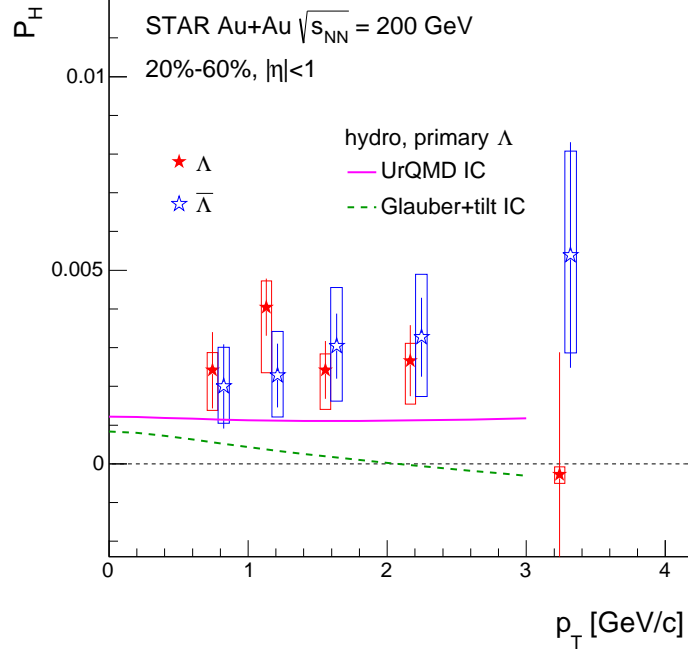


Fig. 26: Polarization of Λ and $\bar{\Lambda}$ as a function of p_T in Au+Au collisions at $\sqrt{s_{NN}} = 200$ GeV. Hydrodynamic model calculations for Λ with two different initial conditions (IC) are compared.

polarized along the magnetic field. Right-handed and left-handed particles have the opposite current but the contribution to the axial current would be the same. Depending on the sign of vector chemical potential μ_v , the sign of the axial current J_5 , therefore the contribution to the polarization, will be flipped. Similar to the Chiral Magnetic Wave study, we might observe this effect by looking at an event-by-event charge asymmetry dependence, assuming $\mu_v/T \propto \frac{N_+ - N_-}{N_+ + N_-}$.

Figure 28 shows the polarization as a function of an event-by-event charge asymmetry A_{ch} in 20%-60% centrality bin. Note that A_{ch} is normalized with its RMS to avoid centrality bias (see Appendix for the detail). The slopes of the A_{ch} dependence seems to be different between Λ and $\bar{\Lambda}$ although the effect is not significant ($1.5-2\sigma$) with given uncertainties.

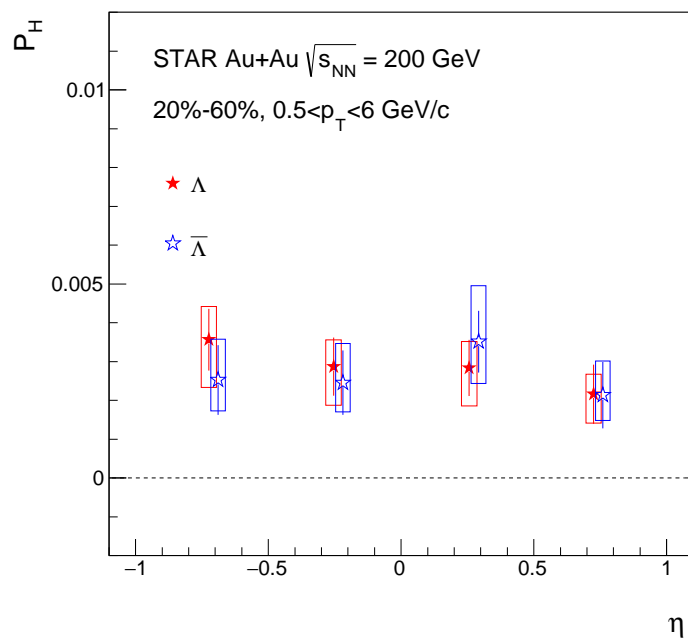


Fig. 27: Polarization of Λ and $\bar{\Lambda}$ as a function of η in Au+Au collisions at $\sqrt{s_{NN}} = 200$ GeV.

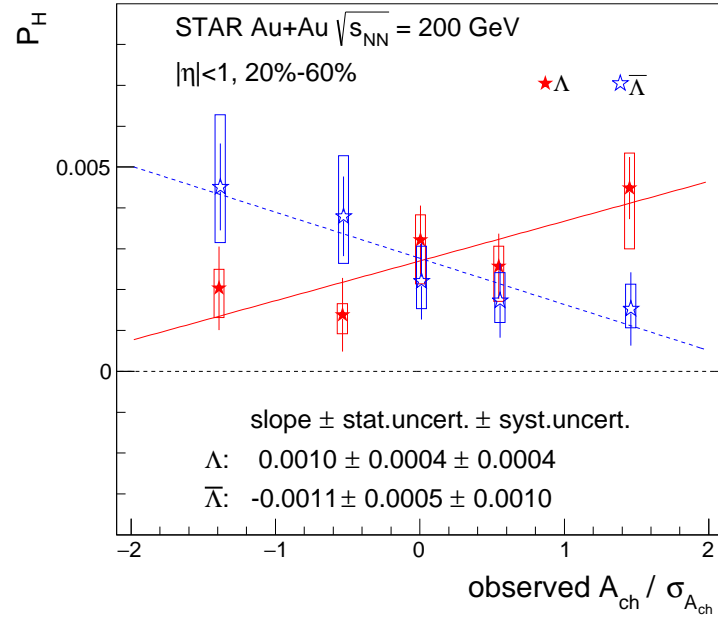


Fig. 28: Polarization of Λ and $\bar{\Lambda}$ as a function of event-by-event charge asymmetry $A_{ch}/\sigma_{A_{ch}}$ in Au+Au collisions at $\sqrt{s_{NN}} = 200$ GeV.

A Run QA for run11 and run14 Au+Au 200 GeV

Figure 29 and 30 show basic variables as a function of run index for run11 and run14 data of Au+Au collisions at $\sqrt{s_{NN}} = 200$ GeV. The study on run10 QA can be found in Ref. [5].

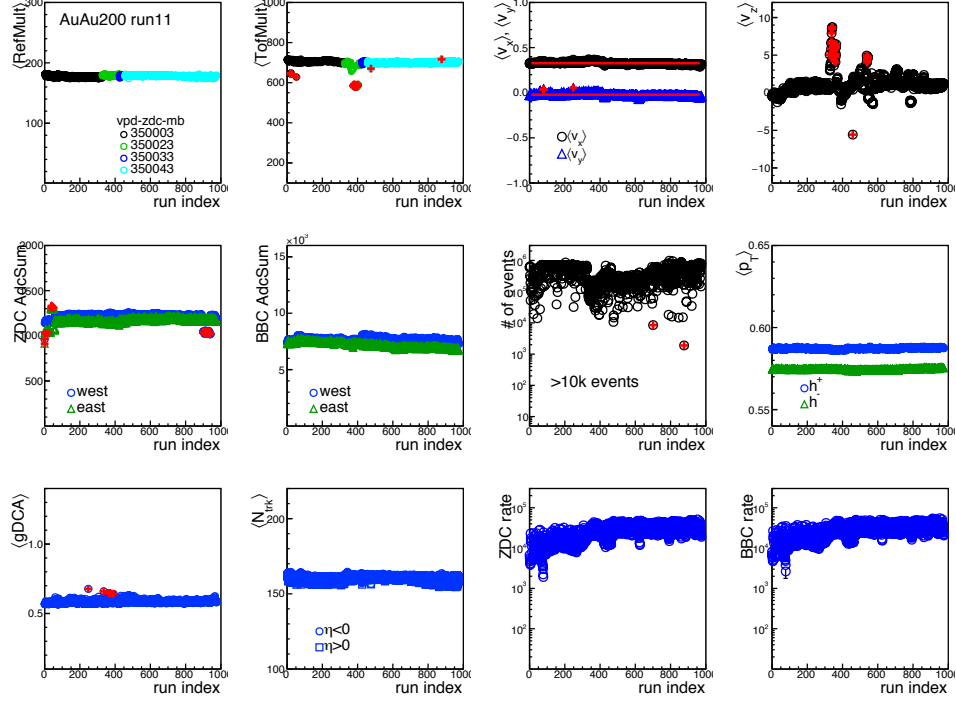


Fig. 29: Run QA plots for run11 Au+Au 200 GeV. Basic variables are plotted as a function of run index, where outliers are determined to be 4σ away from the average and are marked as red cross symbols.

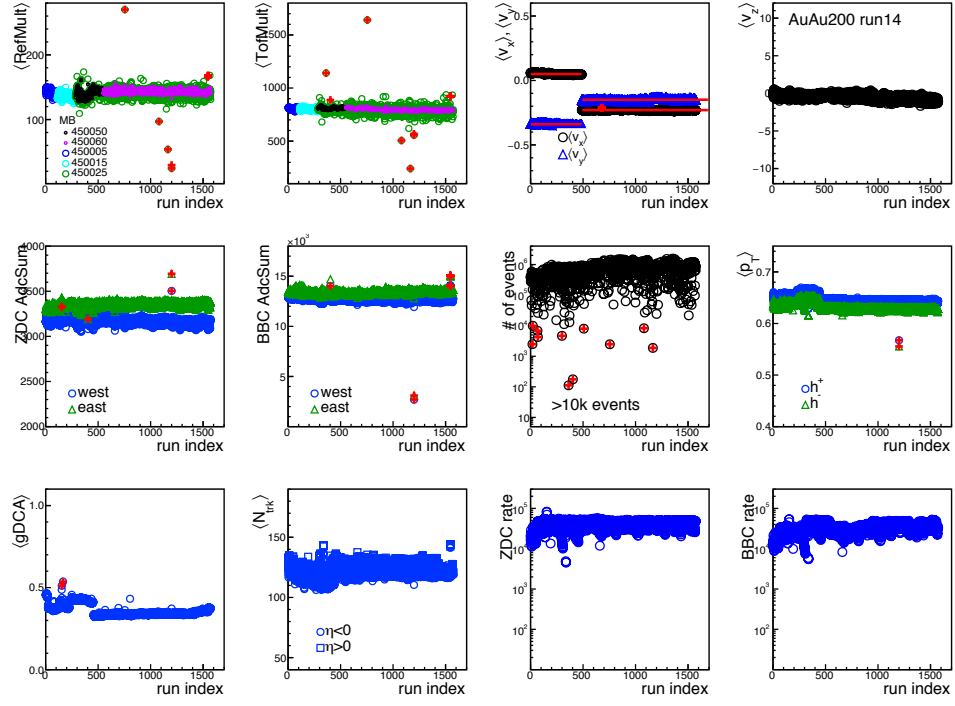


Fig. 30: Run QA plots for run14 Au+Au 200 GeV. Basic variables are plotted as a function of run index, where outliers are determined to be 4σ away from the average and are marked as red cross symbols.

B Calibration of the first-order event plane

As described in Ref. [5], the event plane calibration takes two steps; recentering and flattening corrections, to take into account the detector acceptance effect. The calibration was done by run-by-run basis, each z-vertex group, and each centrality 5% step. Figure 31 and 32 show reconstructed Ψ_1 distributions before and after the corrections.

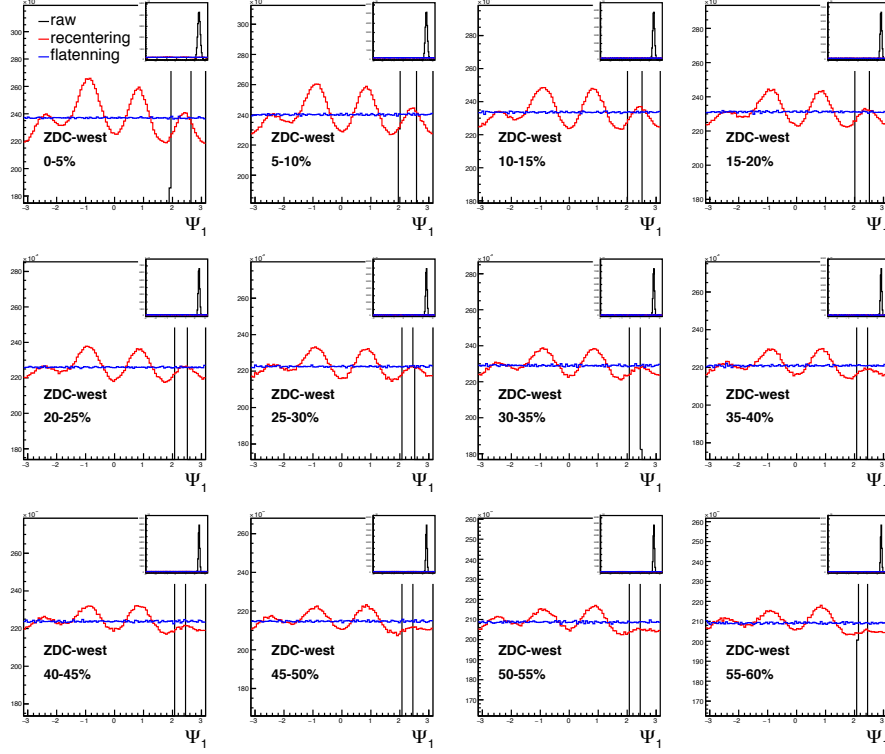


Fig. 31: First-order event plane distribution of ZDC-SMD east-west combined for different centrality bins before and after recentering and flattening corrections in Au+Au collisions at $\sqrt{s_{NN}} = 200$ GeV for run11 data. Inserts in each panel show the same plots as the main panle but with differetn range of y-axis.

Fig. 32: First-order event plane distribution of ZDC-SMD east-west combined for different centrality bins before and after recentering and flattening corrections in Au+Au collisions at $\sqrt{s_{NN}} = 200$ GeV for run14 data. Inserts in each panel show the same plots as the main panle but with differetn range of y-axis.

C More plots on systematic study

In this appendix, relevant plots used to determine the systematic uncertainties are presented (only for run-average results). In most of cases, results from each systematic source are consistent with default result within statistical uncertainties. There was no clear global trend in each systematic source, e.g. all point data points move up (down) compared to default results. Therefore we calculated point-by-point asymmetric systematic uncertainty for each point, e.g. if the result from certain systematic source is larger than the default, the difference was incorporated only for upper limit of the systematic uncertainties. We also prepared plots with symmetric uncertainties, where absolute value of the difference from each systematic source was used to both lower and upper uncertainties. However in this case the uncertainties would be overestimated. As mentioned in the main text, the standard deviation was used for the uncertainty from topological cuts. For the event plane determination, average of differences from ZDCSMD east and west was used for the symmetric uncertainty. Figure 33-37 are for centrality dependence, Fig. 40-44 for p_T dependence, Fig. 51-51 for η dependence, and Fig. 58-58 for A_{ch} dependence. Figure 38, Fig. 45, Fig. 52, and Fig. 59 show results with asymmetric and symmetric systematic uncertainties. Figure 39, 46, 53, and 60 present results of Λ polarization showing contributions from each systematic source, for both asymmetric and symmetric uncertainties.

We notice that our systematic uncertainties are dominated by statistical fluctuations, but still employed them to final results as a conservative estimate.

C.1 Centrality dependence

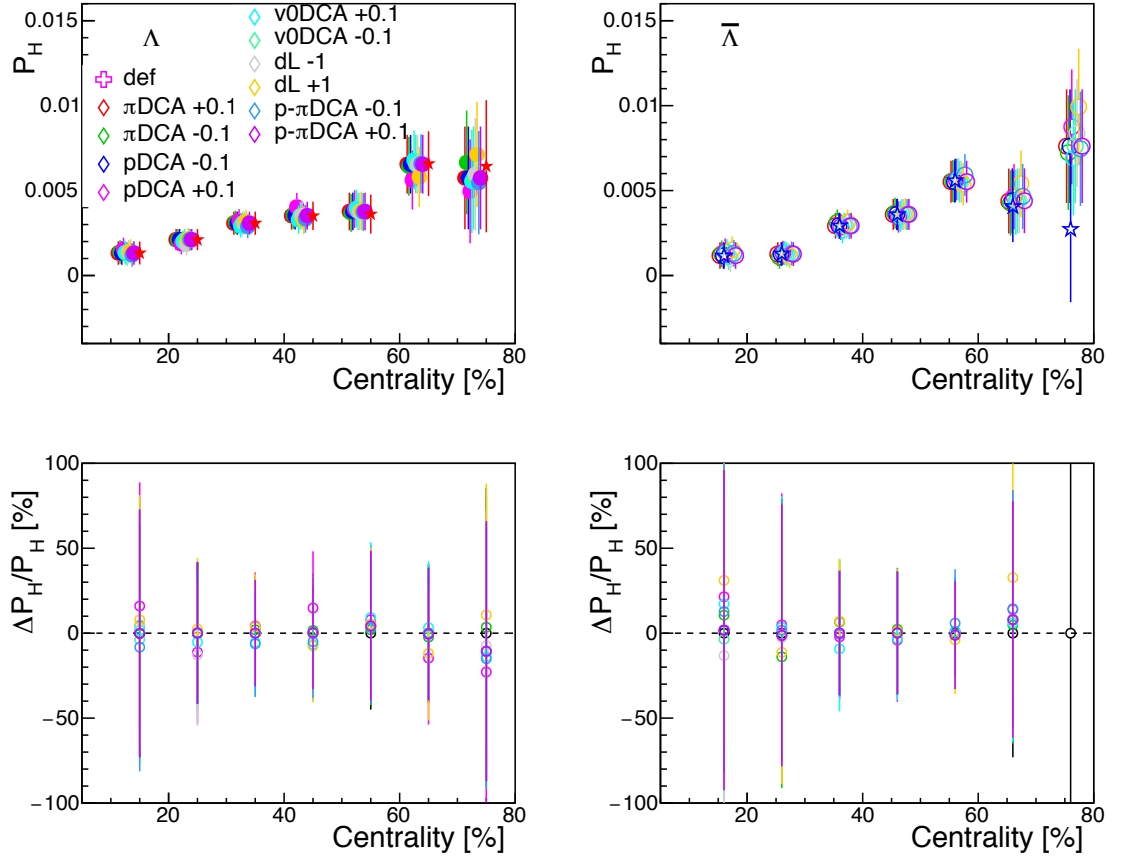


Fig. 33: Centrality dependence of polarization for Λ and $\bar{\Lambda}$ with different topological cuts and the difference from default condition in percentile.

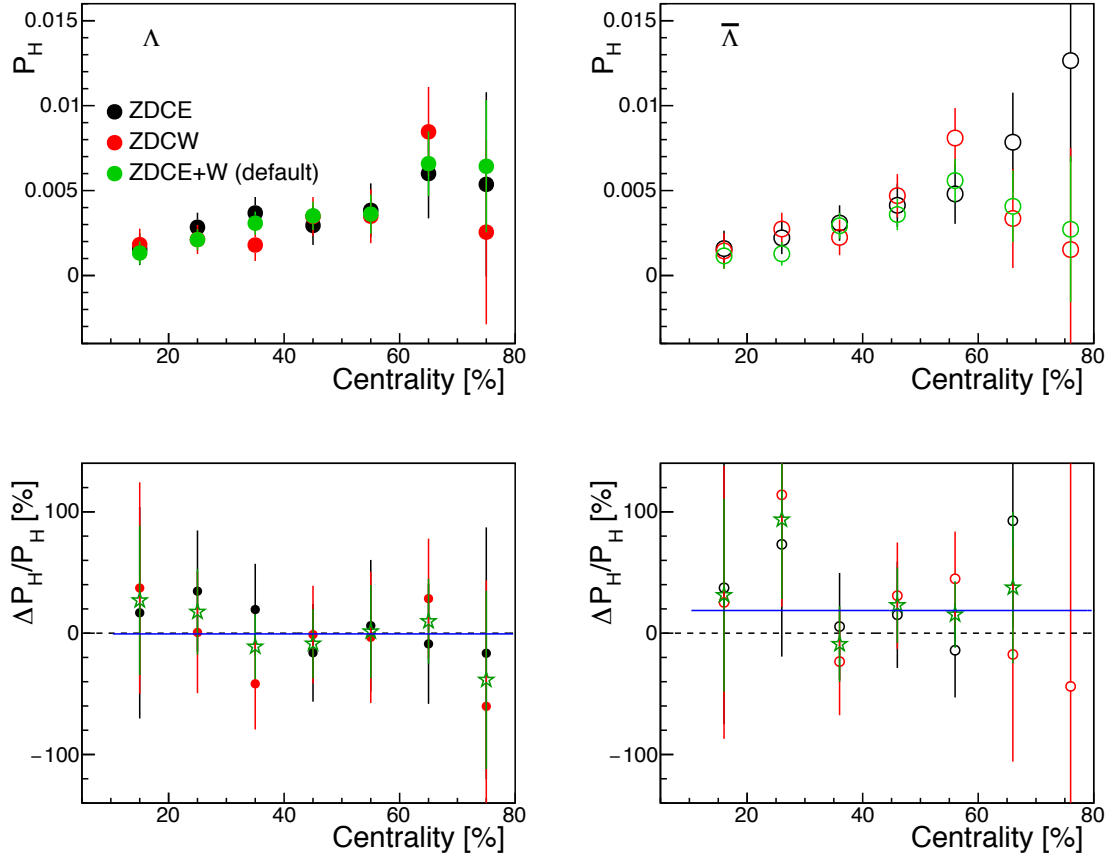


Fig. 34: Centrality dependence of polarization for Λ and $\bar{\Lambda}$ measured with different event planes and the difference from default condition in percentile.

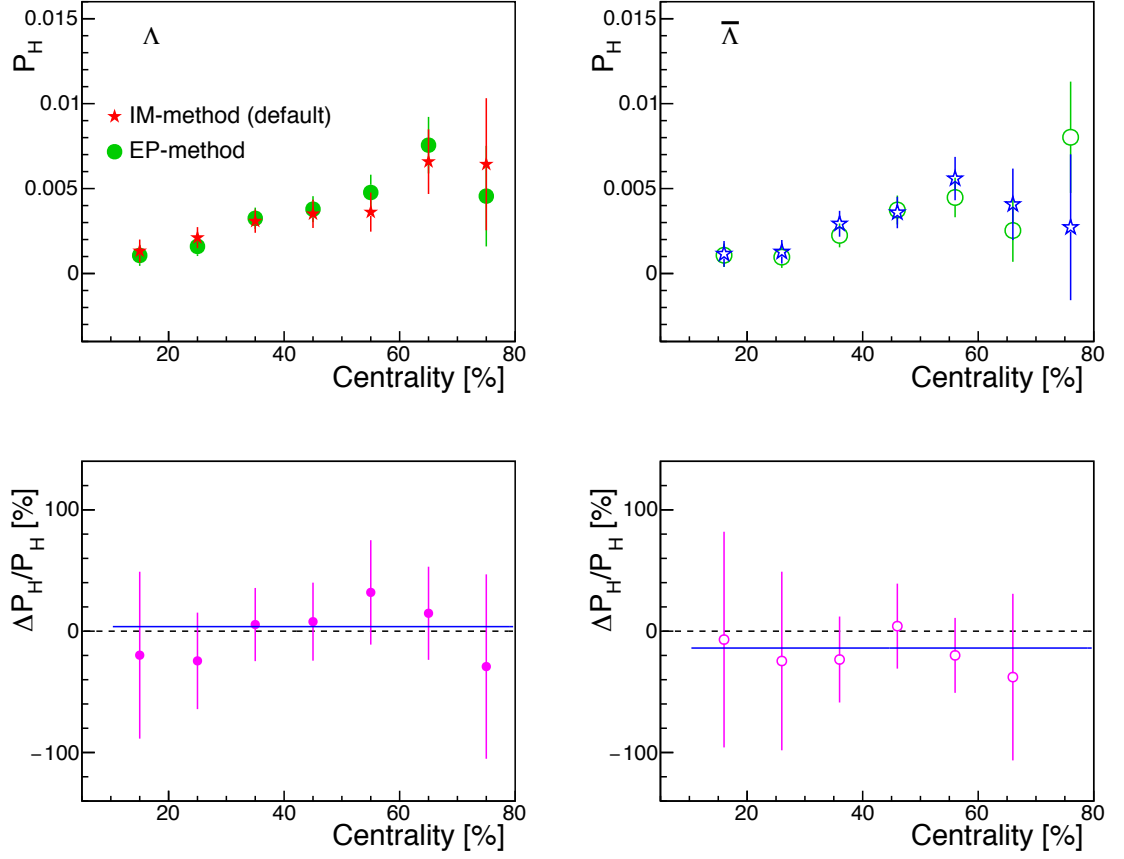


Fig. 35: Centrality dependence of polarization for Λ and $\bar{\Lambda}$ measured with the invariant mass method and event plane method and the difference from default condition in percentile.

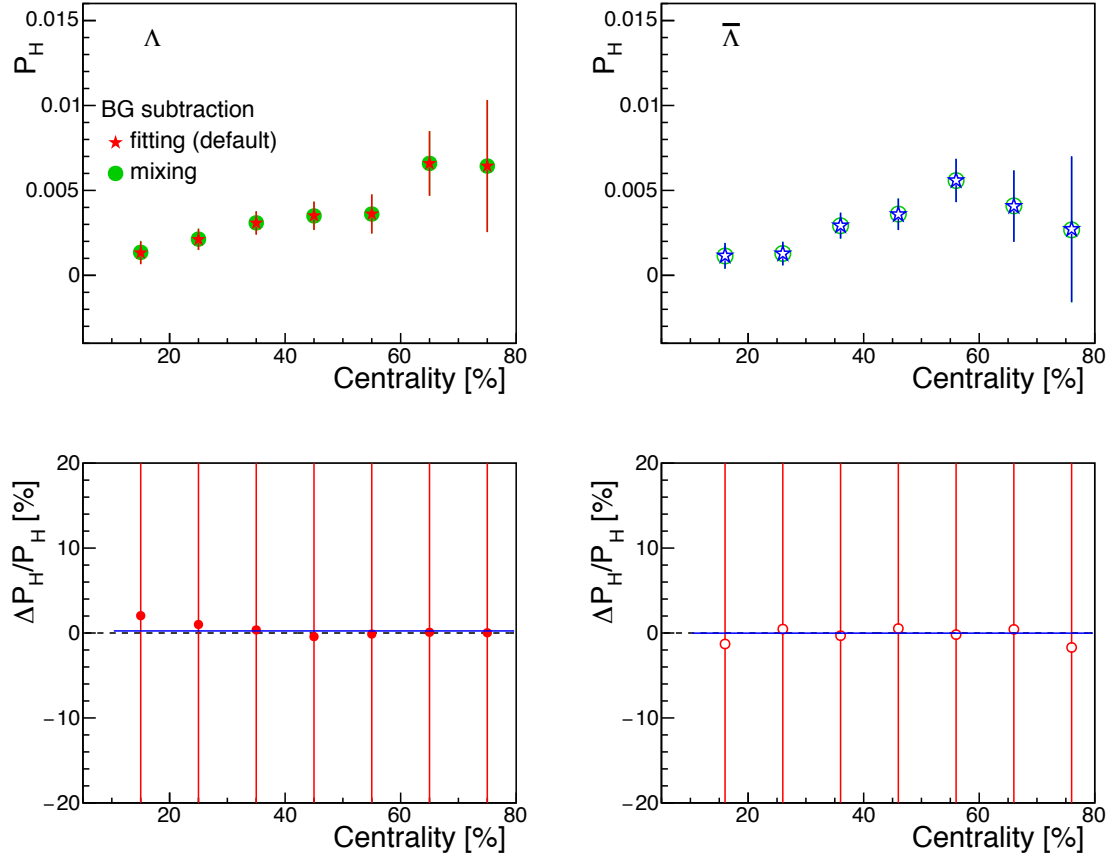


Fig. 36: Centrality dependence of polarization for Λ and $\bar{\Lambda}$ measured with different background subtractions in Λ reconstruction and the difference from default condition in percentile.

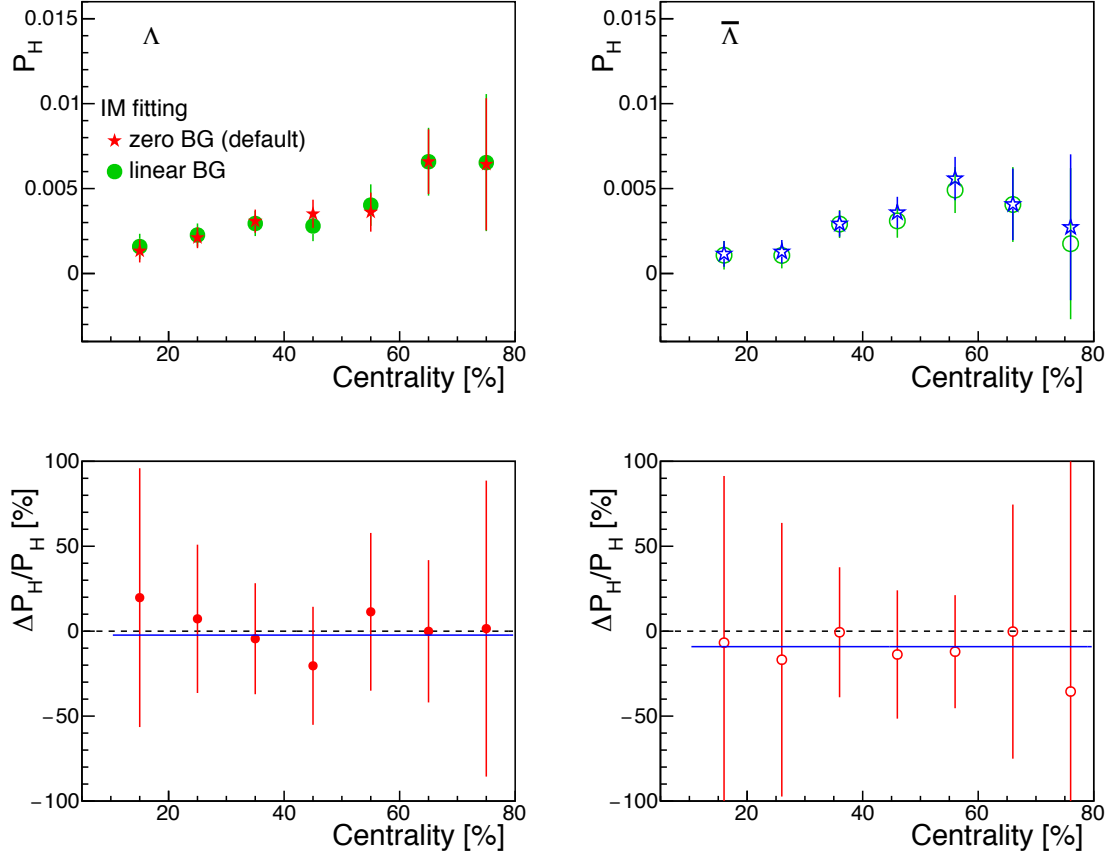


Fig. 37: Centrality dependence of polarization for Λ and $\bar{\Lambda}$ measured with fitting functions for the invariant mass method and the difference from default condition in percentile.

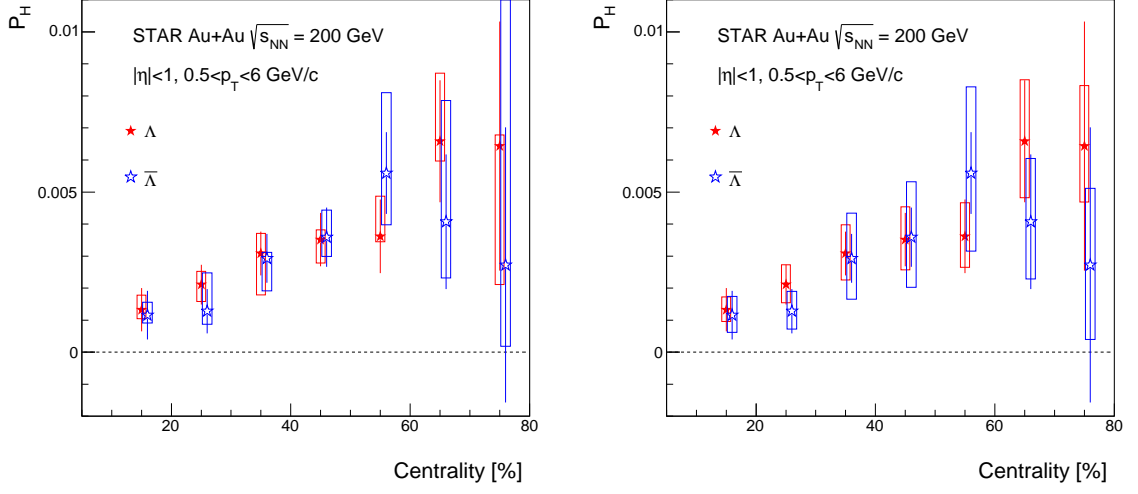


Fig. 38: Centrality dependence of polarization for Λ and $\bar{\Lambda}$ with two different calculations of systematic uncertainties. Left plot is for point-by-point asymmetric systematic uncertainties and right for fitting procedure.

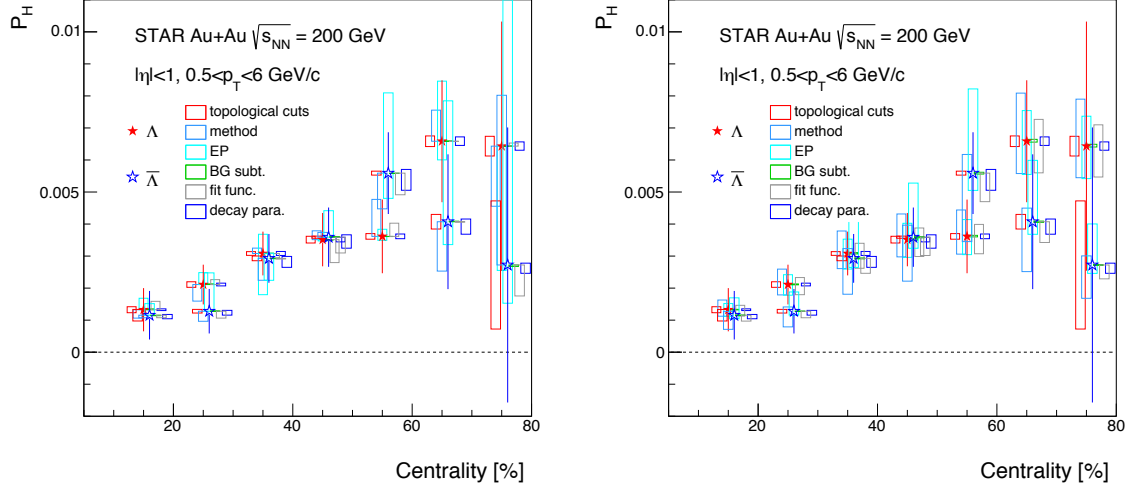


Fig. 39: Centrality dependence of polarization for Λ showing each systematic source. Left plot is for point-by-point asymmetric systematic uncertainties and right for fitting procedure.

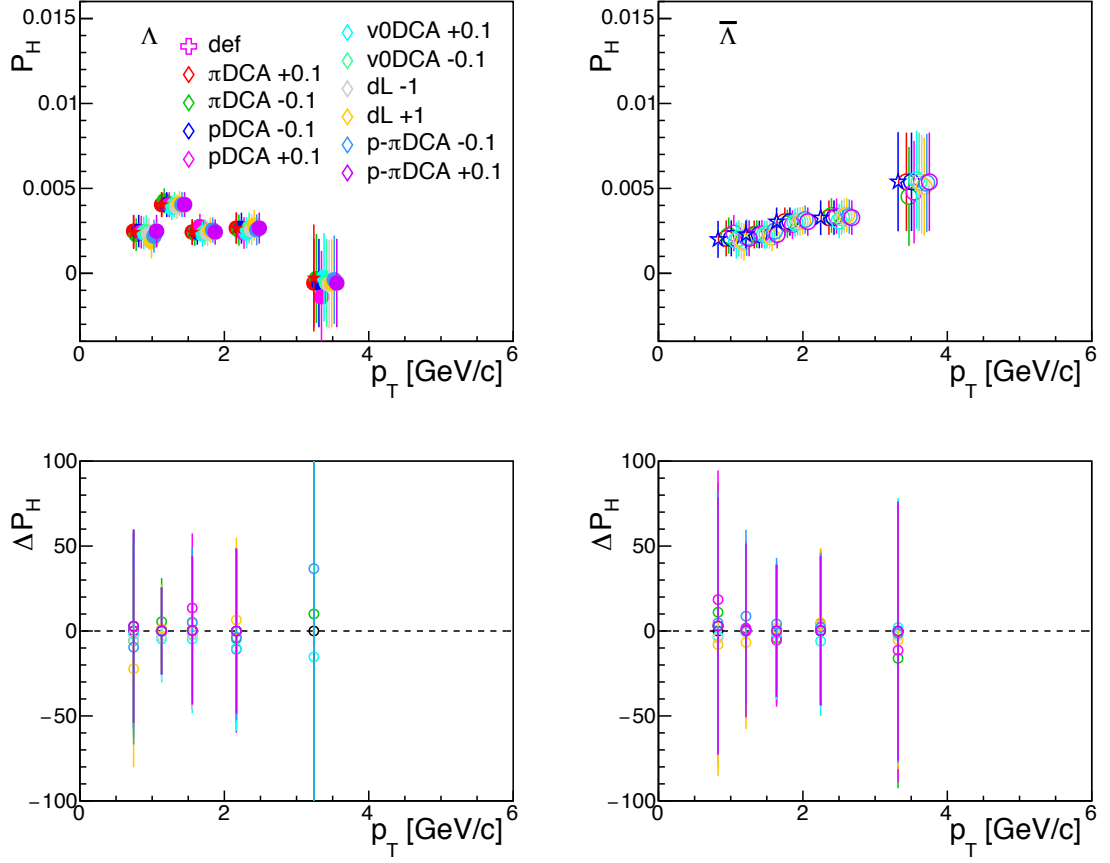
C.2 p_T dependence

Fig. 40: p_T dependence of polarization for Λ and $\bar{\Lambda}$ with different topological cuts and the difference from default condition in percentile.

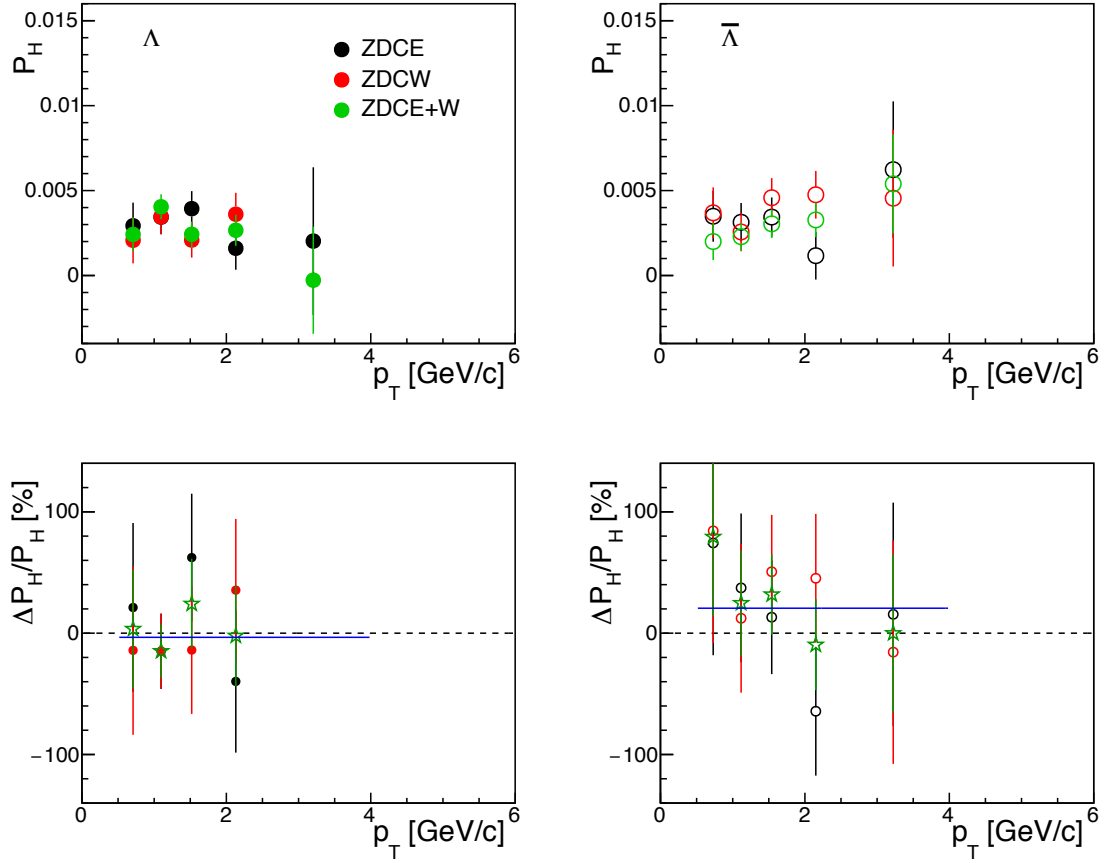


Fig. 41: p_T dependence of polarization for Λ and $\bar{\Lambda}$ measured with different event planes and the difference from default condition in percentile.

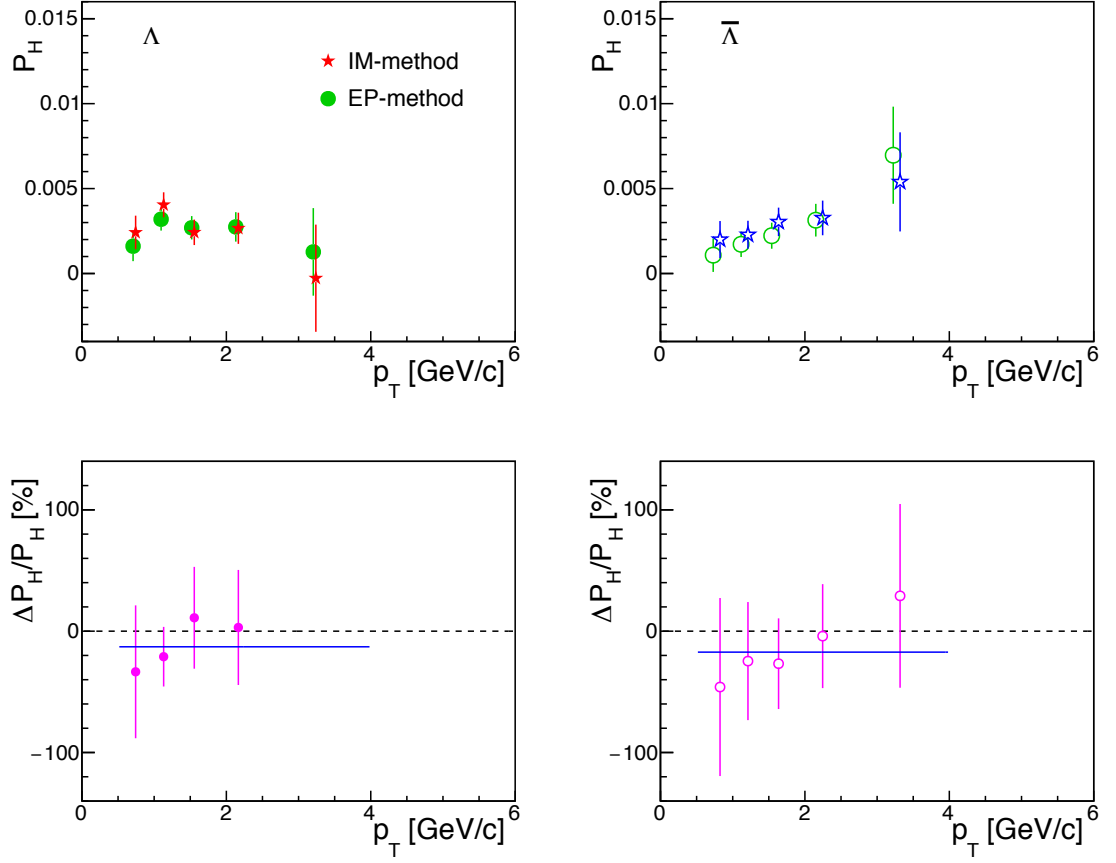


Fig. 42: p_T dependence of polarization for Λ and $\bar{\Lambda}$ measured with the invariant mass method and event plane method and the difference from default condition in percentile.

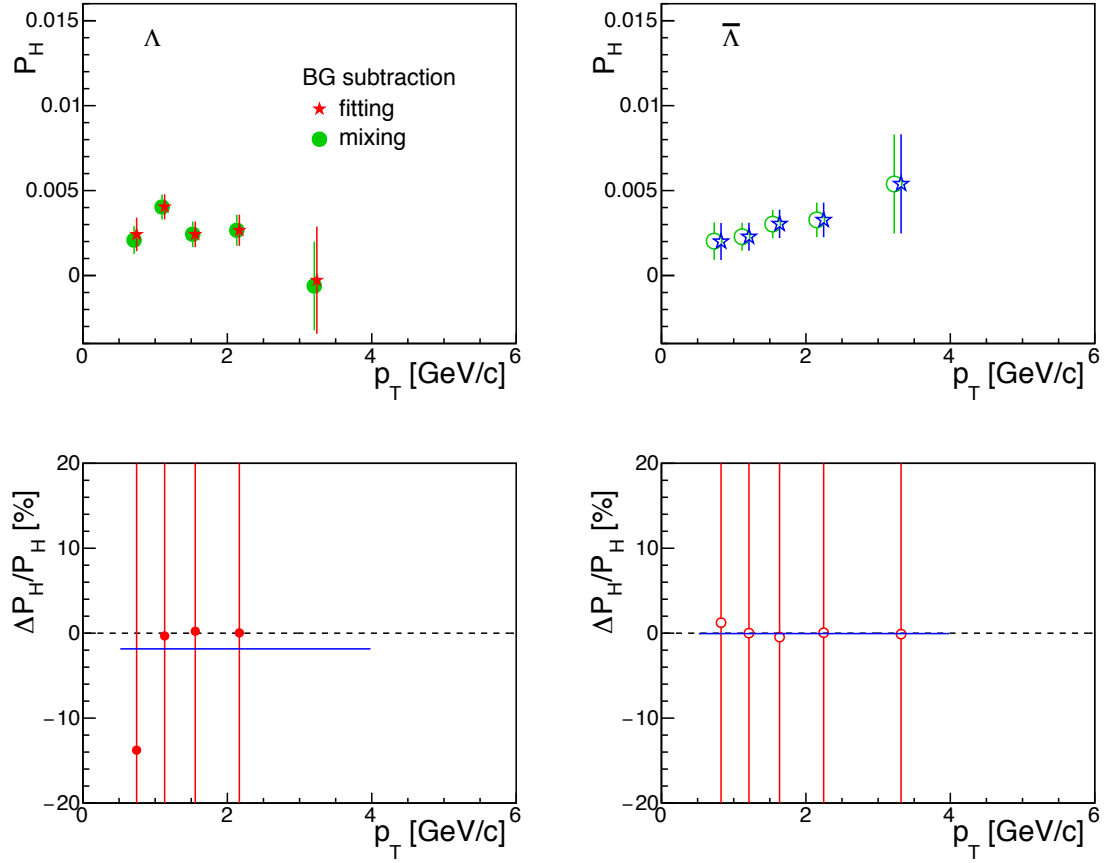


Fig. 43: p_T dependence of polarization for Λ and $\bar{\Lambda}$ measured with different background subtractions in Λ reconstruction and the difference from default condition in percentile.

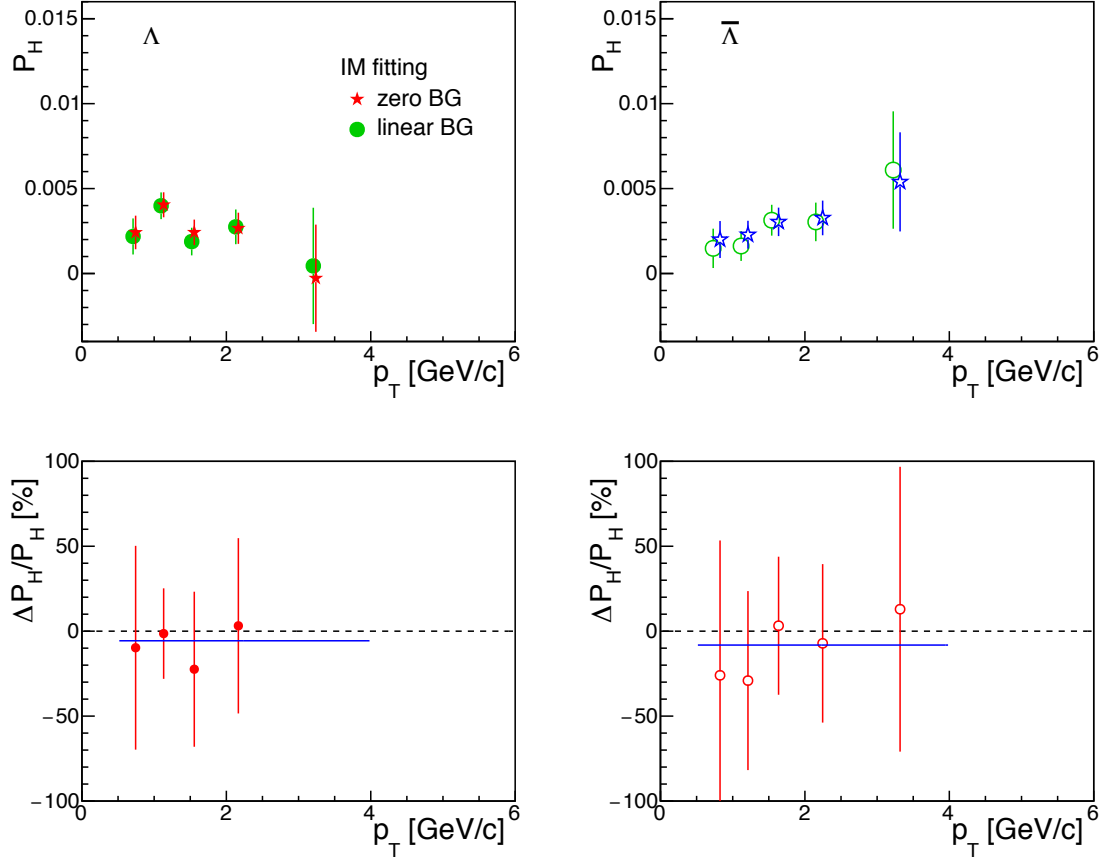


Fig. 44: p_T dependence of polarization for Λ and $\bar{\Lambda}$ measured with fitting functions for the invariant mass method and the difference from default condition in percentile.

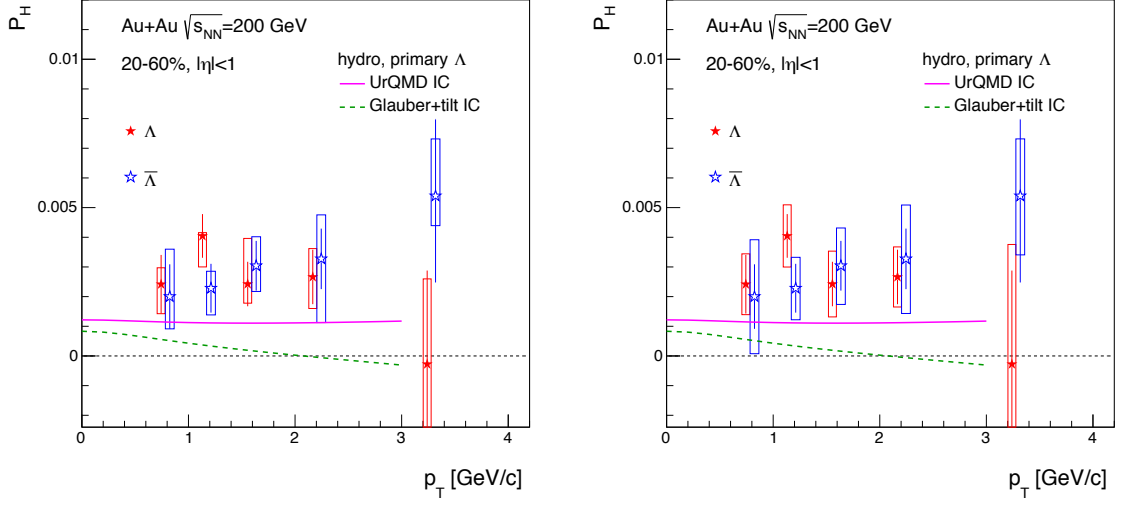


Fig. 45: p_T dependence of polarization for Λ and $\bar{\Lambda}$ with two different calculations of systematic uncertainties. Left plot is for point-by-point asymmetric systematic uncertainties and right for fitting procedure.

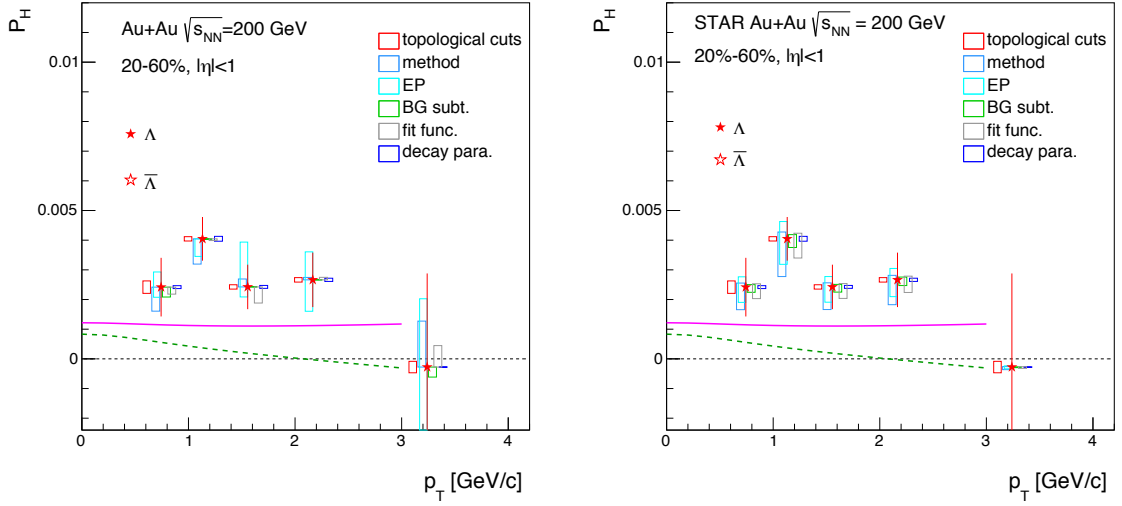


Fig. 46: p_T dependence of polarization for Λ showing each systematic source. Left plot is for point-by-point asymmetric systematic uncertainties and right for fitting procedure.

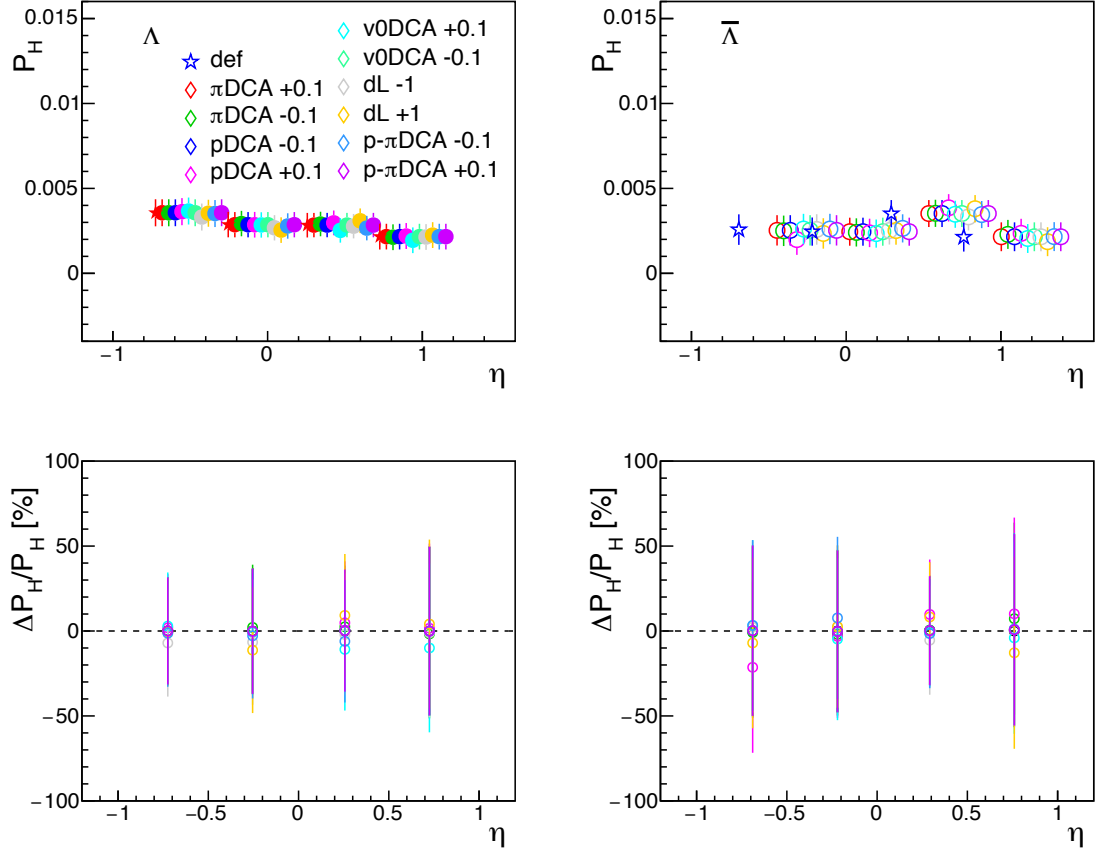
C.3 η dependence

Fig. 47: η dependence of polarization for Λ and $\bar{\Lambda}$ with different topological cuts and the difference from default condition in percentile.

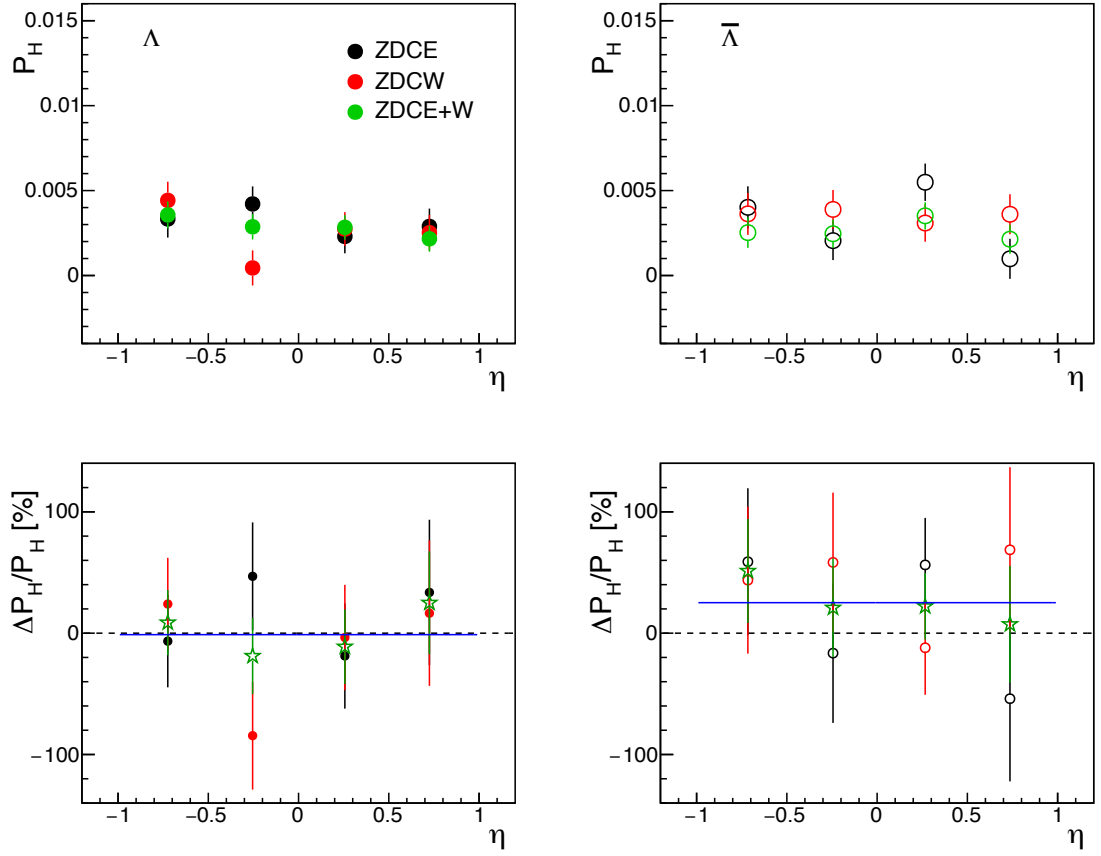


Fig. 48: η dependence of polarization for Λ and $\bar{\Lambda}$ measured with different event planes and the difference from default condition in percentile.

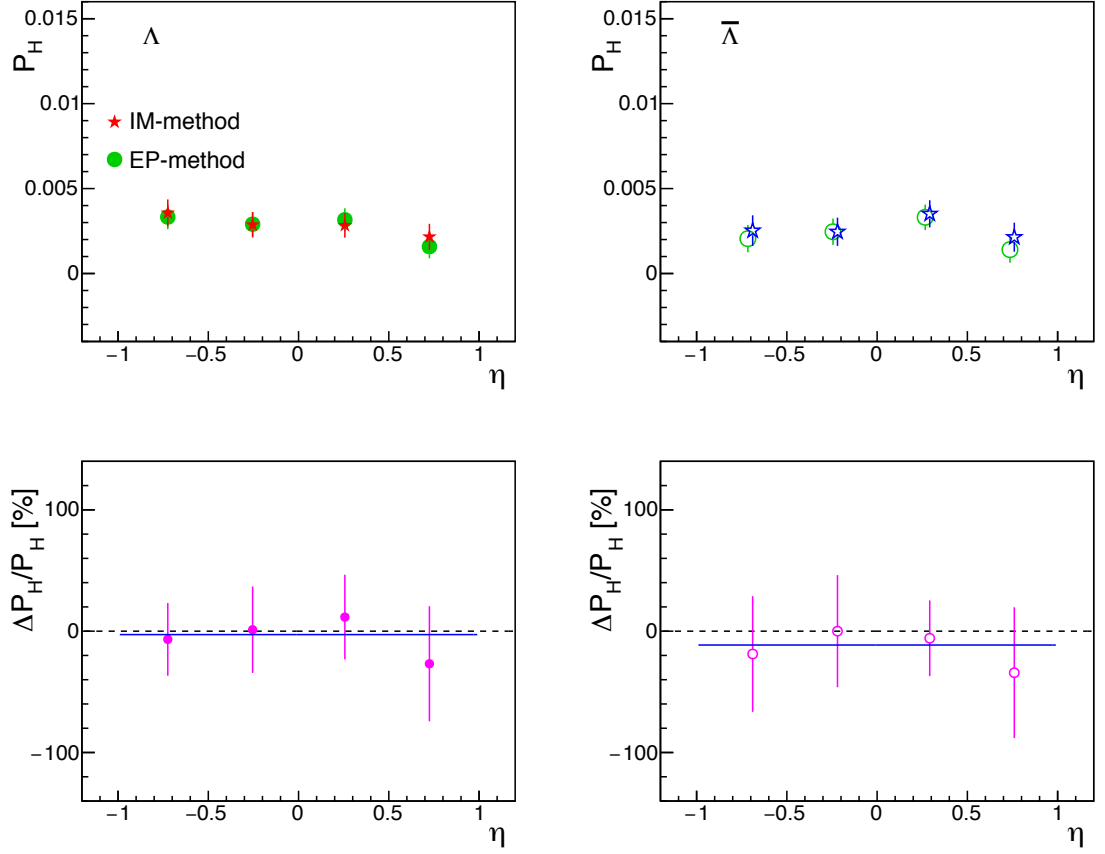


Fig. 49: η dependence of polarization for Λ and $\bar{\Lambda}$ measured with the invariant mass method and event plane method and the difference from default condition in percentile.

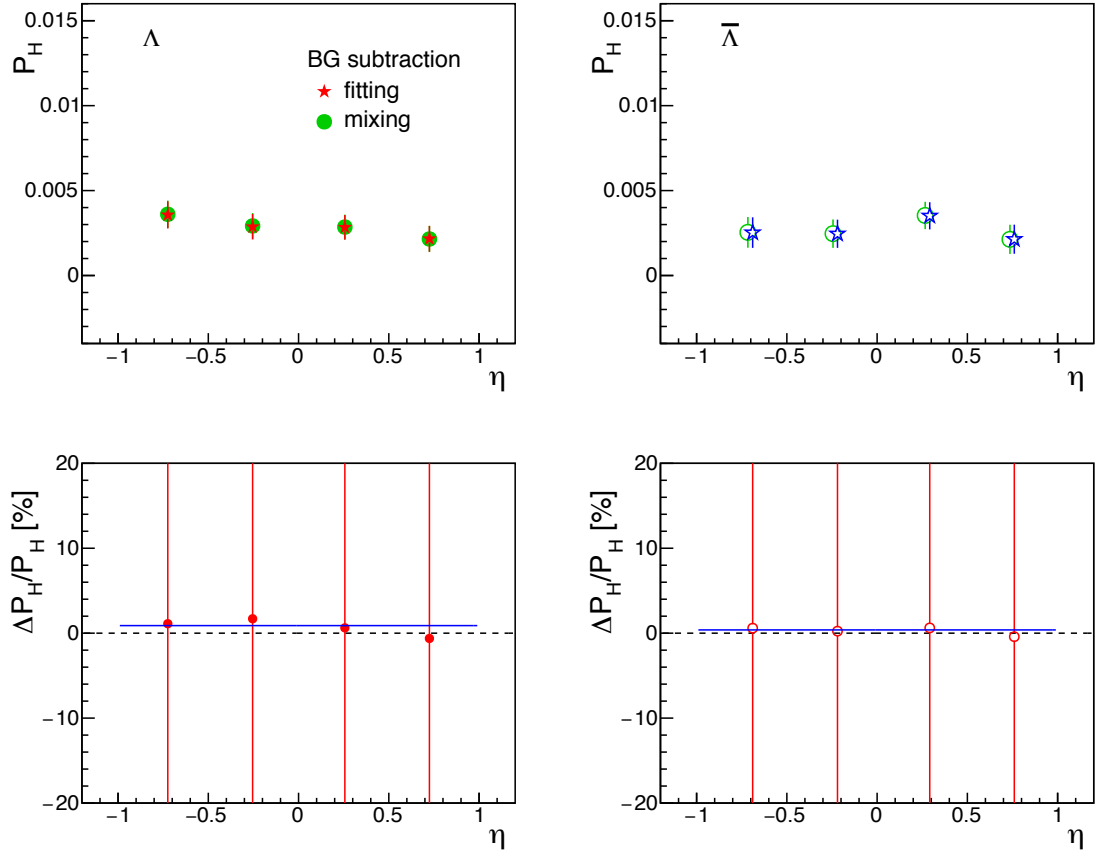


Fig. 50: η dependence of polarization for Λ and $\bar{\Lambda}$ measured with different background subtractions in Λ reconstruction and the difference from default condition in percentile.

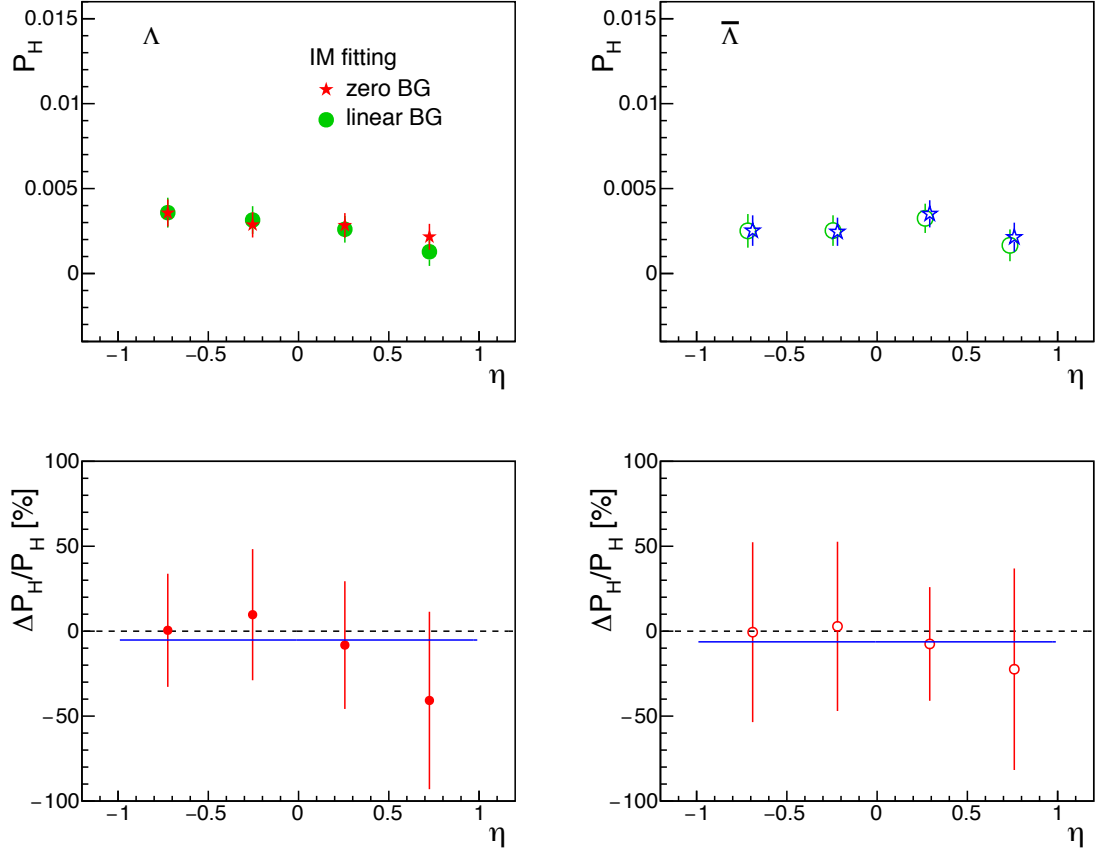


Fig. 51: η dependence of polarization for Λ and $\bar{\Lambda}$ measured with fitting functions for the invariant mass method and the difference from default condition in percentile.

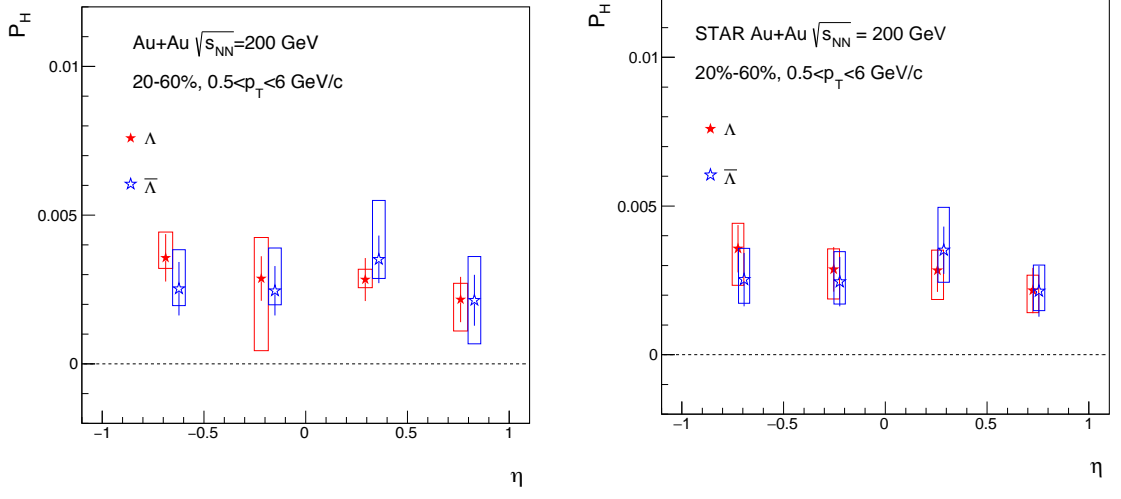


Fig. 52: η dependence of polarization for Λ and $\bar{\Lambda}$ with two different calculations of systematic uncertainties. Left plot is for point-by-point asymmetric systematic uncertainties and right for fitting procedure.

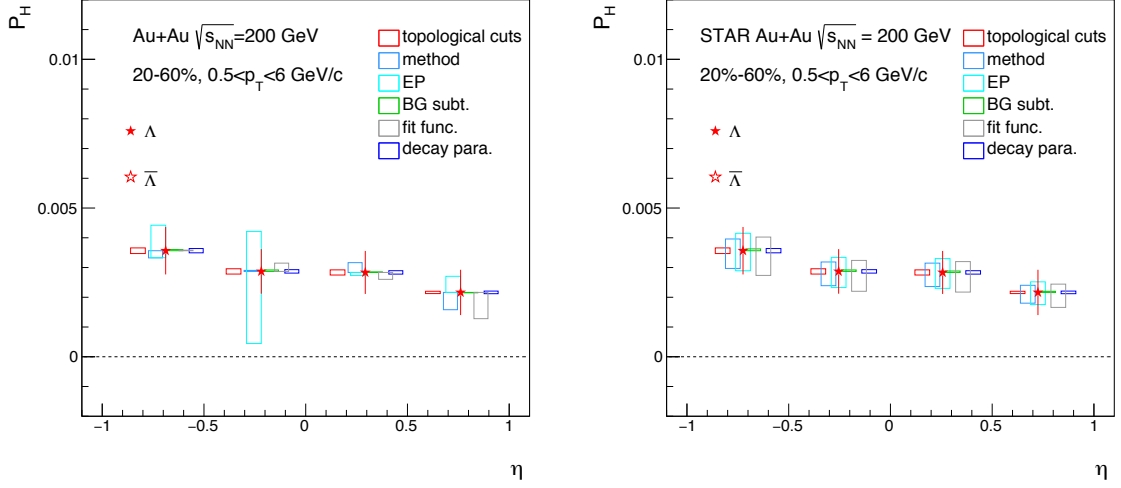


Fig. 53: η dependence of polarization showing each systematic source. Left plot is for point-by-point asymmetric systematic uncertainties and right for fitting procedure.

C.4 A_{ch} dependence

Left panel in Fig. 54 shows A_{ch} distributions for different centrality bins. As you can see, widths of A_{ch} distributions differ with centrality. Since the polarization shows a clear centrality dependence, we need to take into account the width to avoid a centrality bias in each A_{ch} bin. Therefore we divided the A_{ch} distributions with their RMS as shown in right panel of Fig. 54.

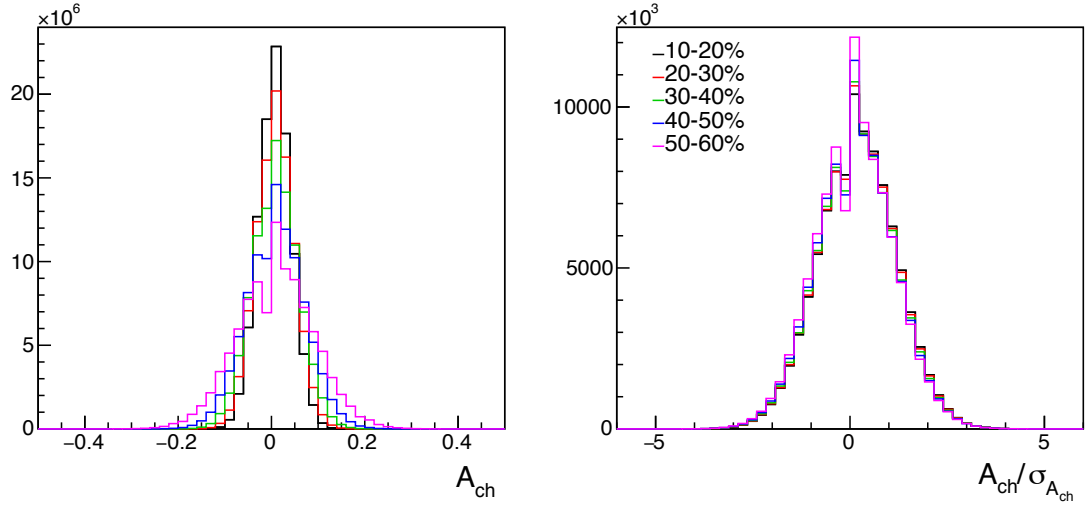


Fig. 54: A_{ch} distributions (left) and A_{ch} normalized with its RMS, $A_{\text{ch}}/\sigma_{A_{\text{ch}}}$ (right), for different centrality bins.

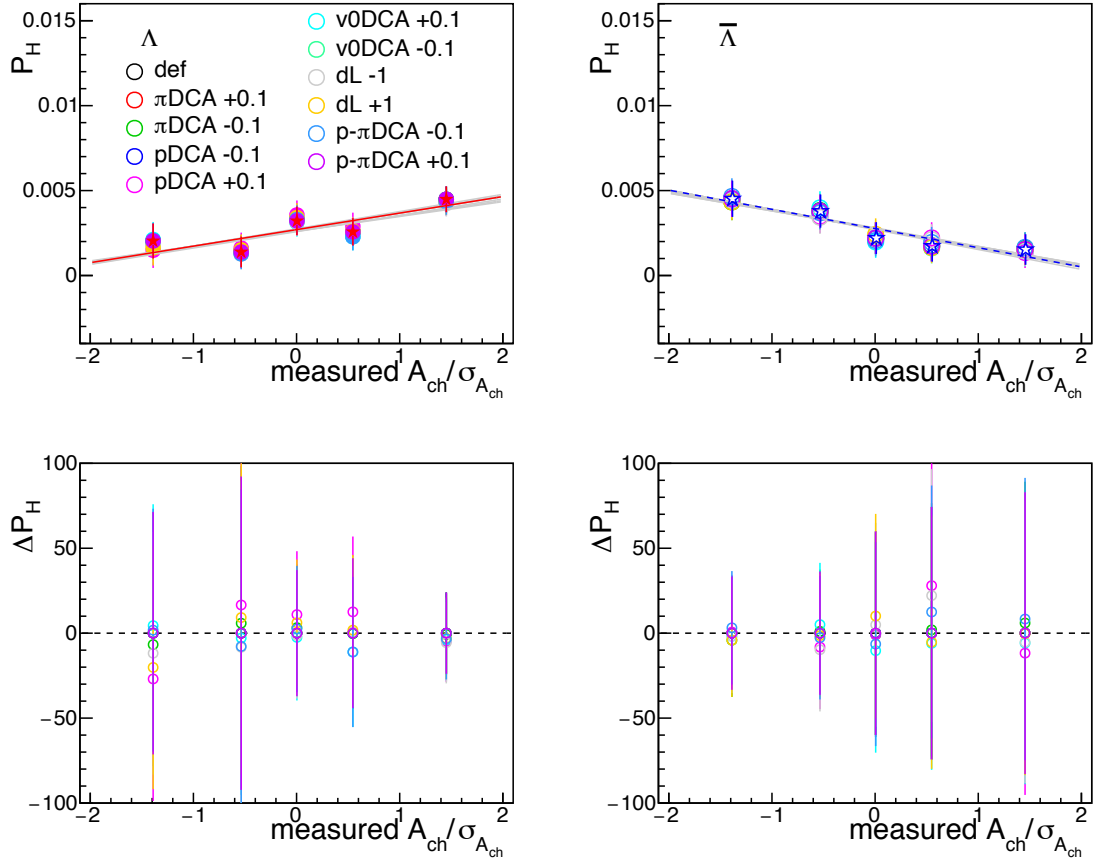


Fig. 55: A_{ch} dependence of polarization for Λ and $\bar{\Lambda}$ with different topological cuts and the difference from default condition in percentile.

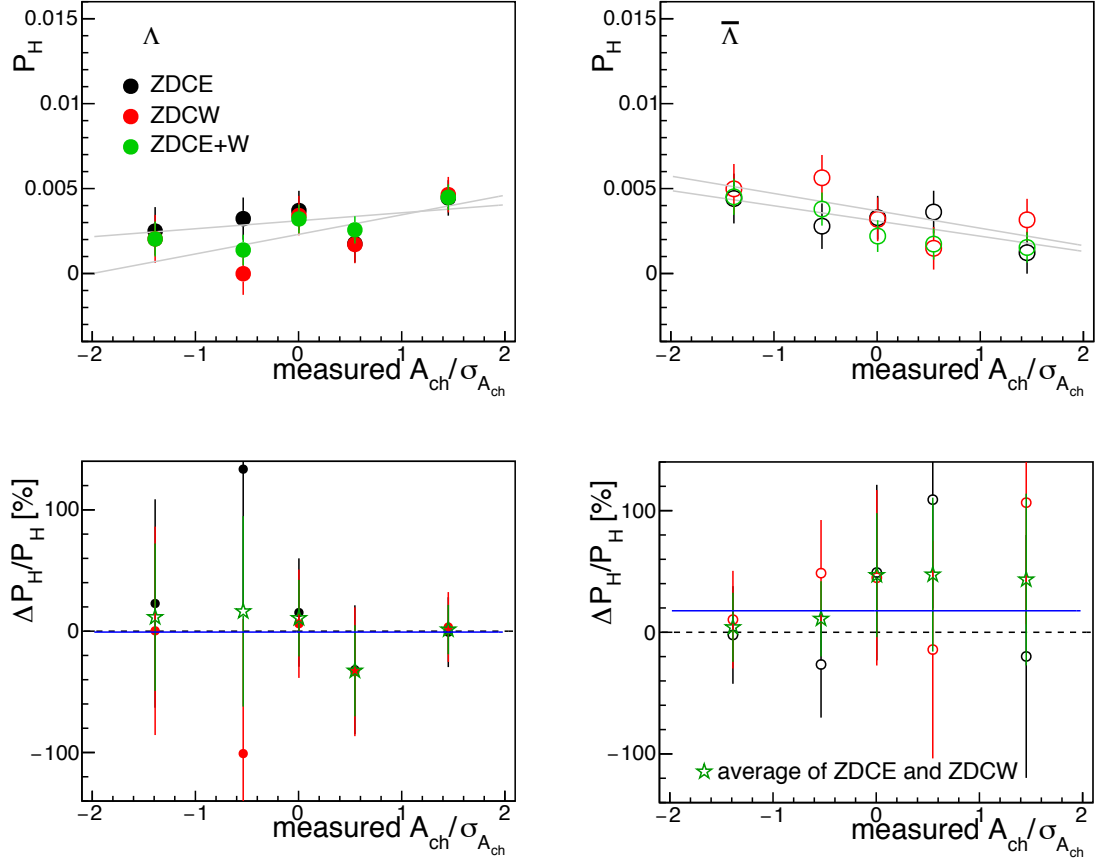


Fig. 56: A_{ch} dependence of polarization for Λ and $\bar{\Lambda}$ measured with different event planes and the difference from default condition in percentile.

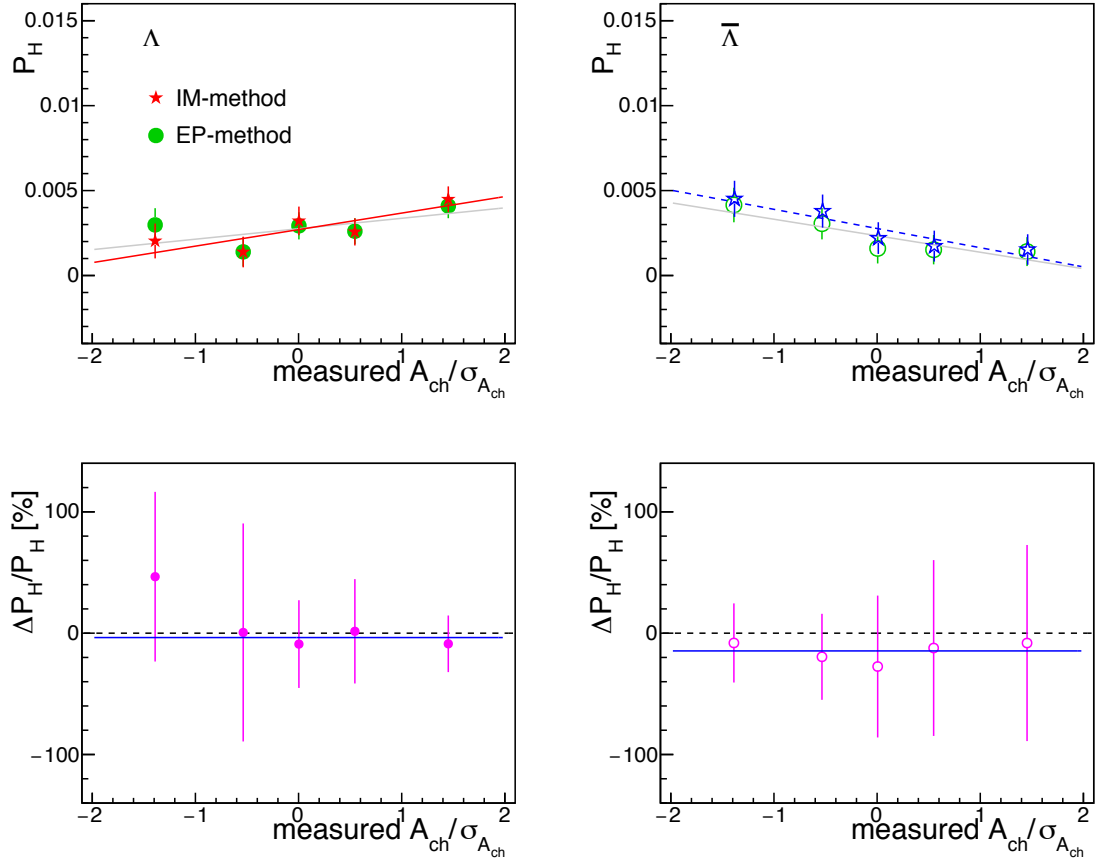


Fig. 57: A_{ch} dependence of polarization for Λ and $\bar{\Lambda}$ measured with the invariant mass method and event plane method and the difference from default condition in percentile.

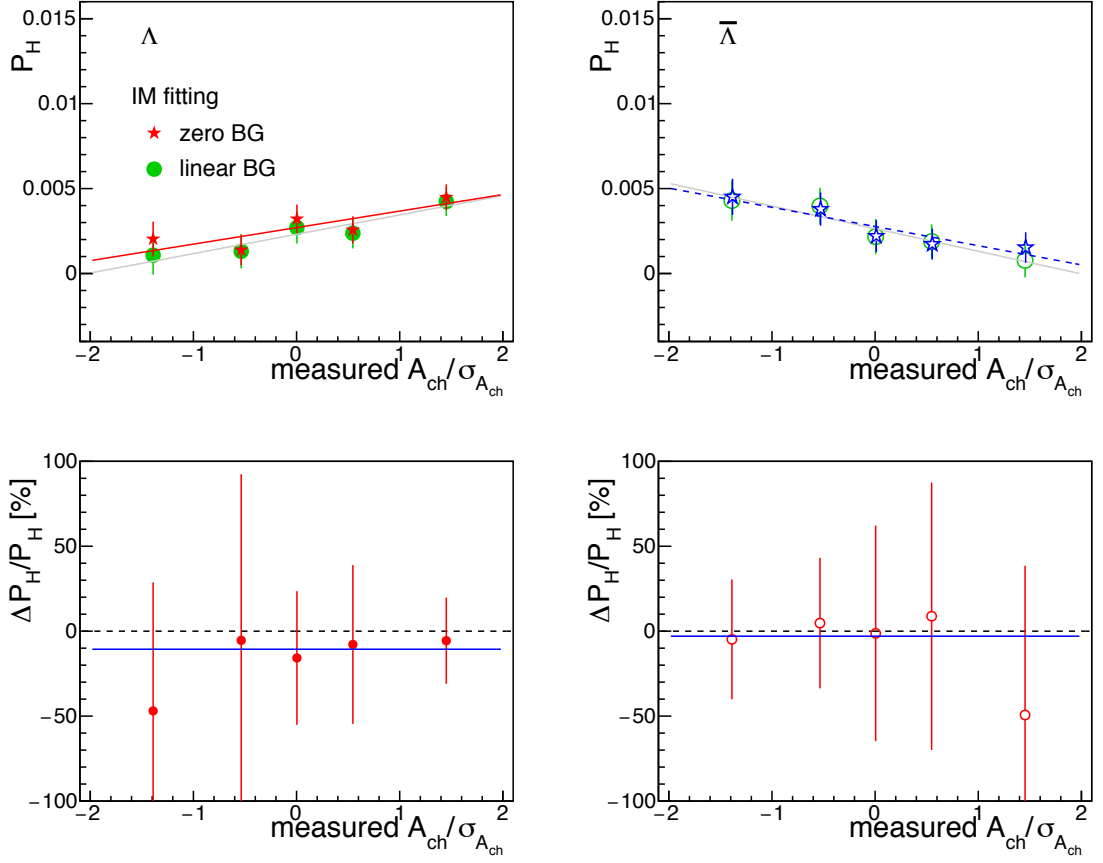


Fig. 58: A_{ch} dependence of polarization for Λ and $\bar{\Lambda}$ measured with fitting functions for the invariant mass method and the difference from default condition in percentile.

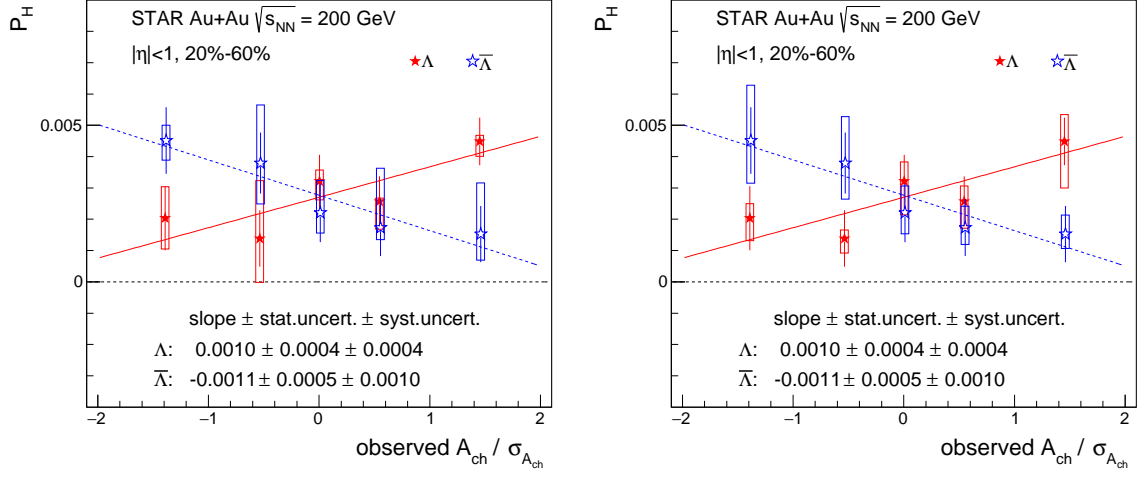


Fig. 59: A_{ch} dependence of polarization for Λ and $\bar{\Lambda}$ with two different calculations of systematic uncertainties. Left plot is for asymmetric point-by-point systematic uncertainties and right for fitting procedure.

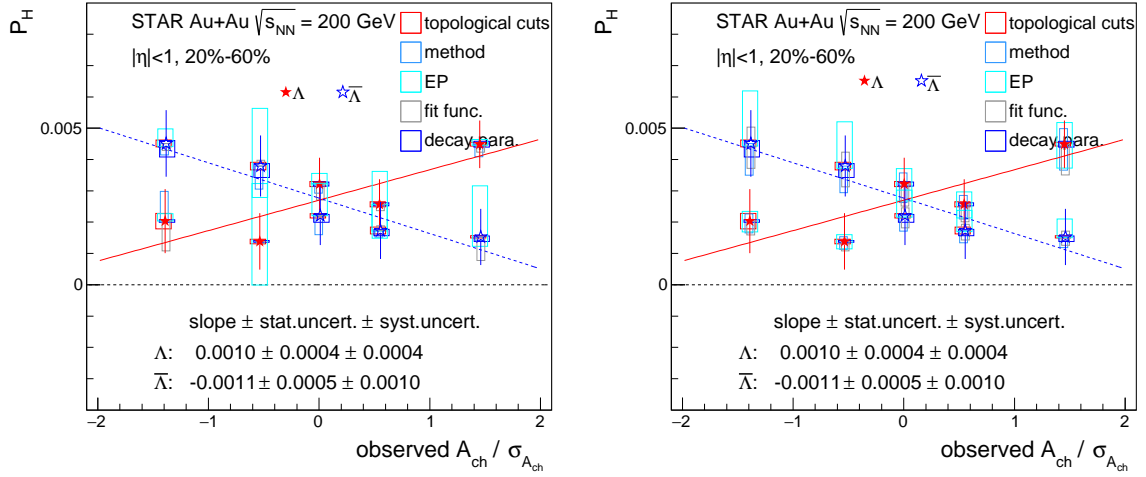


Fig. 60: A_{ch} dependence of polarization showing each systematic source. Left plot is for asymmetric point-by-point systematic uncertainties and right for fitting procedure.

D Addendum to the event plane method

Since $(\Psi_1 - \phi_p^*)$ distributions as shown in Fig. 5 are not simple sine curves, we did additional checks to understand the structure. Figure 62 shows $(\Psi_1 - \phi_p^*)$ distributions of Λ and $\bar{\Lambda}$ after the background subtraction in 10%-60% centrality bin. To extract a raw signal of polarization $\langle \sin(\Psi_1 - \phi_p^*) \rangle$, we fitted the data with $p_0(1 + 2p_1 \sin(\Delta\phi))$ where $\Delta\phi = \Psi_1 - \phi_p^*$. We also included the cosine terms for test; $p_0(1 + 2p_1 \sin(\Delta\phi) + 2 \sum_{n=2}^{n \leq 4} p_{n,c} \cos(n\Delta\phi))$. As shown in the figure, the extracted p_1 was found to not change even if we included the cosine terms and the overall shape of the distribution can be explained by $\cos(2\Delta\phi)$ term. Figure ?? the same plot but for off-mass region, i.e. combinatorial background. We confirmed that parameter p_1 was consistent with zero and only cosine $2\Delta\phi$ term appears.

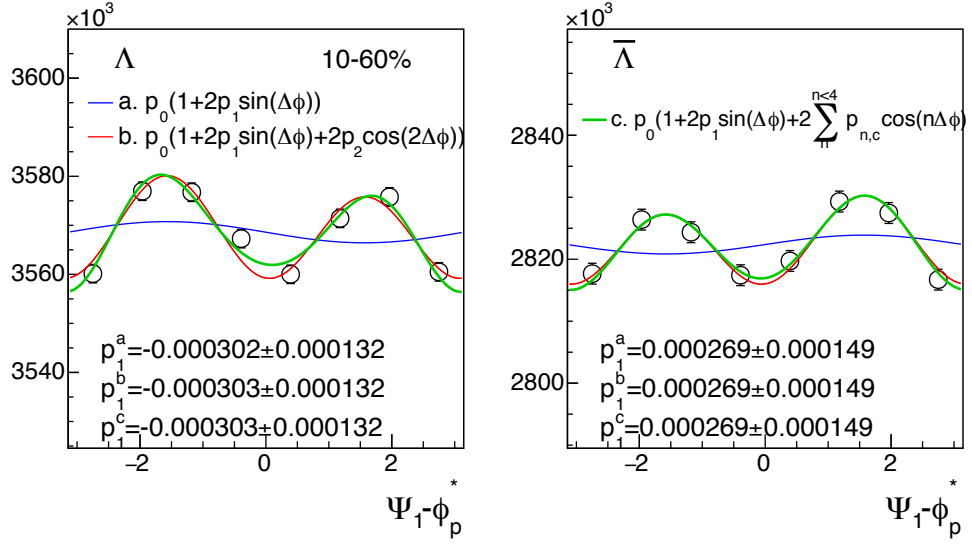


Fig. 61: $(\Psi_1 - \phi_p^*)$ distributions for Λ and $\bar{\Lambda}$ after background subtraction in 10%-60% centrality bin. Solid lines show fitting functions as indicated in the figure. Extracted fitting results of a coefficient p_1 are also shown together.

The second-order coefficient in the cosine terms, p_2 , shows negative value unlike the elliptic flow v_2 measured in normal ways. This would be due to the decay kinematics and STAR acceptance effects. In Fig. 63, p_T dependence of measured p_2 is shown. To take into account such an effect from the kinematics, the p_2 was divided by $\langle \cos(2\phi_\Lambda - 2\phi_p^*) \rangle$ and also the event plane resolution, comparing to v_2 measured with the first-order event plane from ZDCSMD. We confirmed that both v_2 roughly agree with each other.

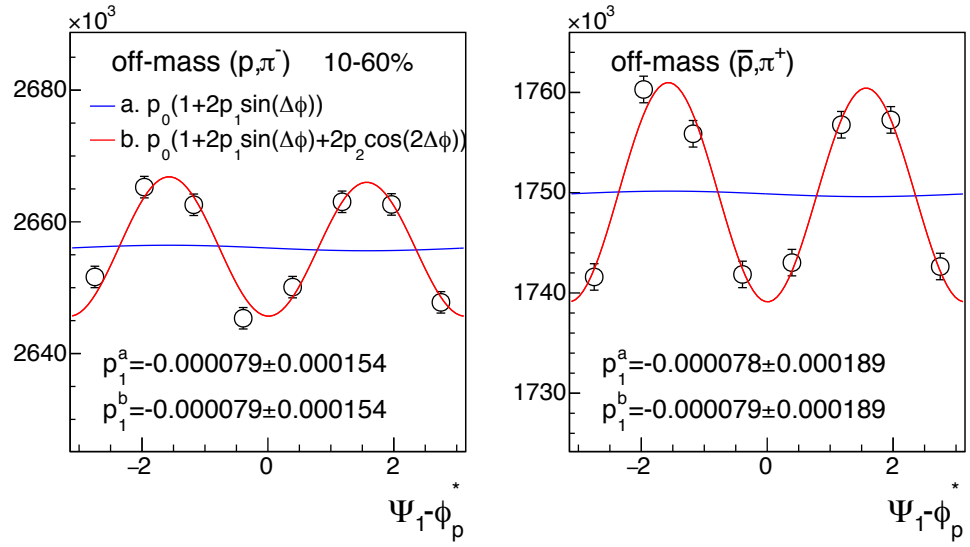


Fig. 62: $(\Psi_1 - \phi_p^*)$ distributions for off-mass region in 10%-60% centrality bin. Solid lines show fitting functions as indicated in the figure. Extracted fitting results of a coefficient p_1 are also shown together.

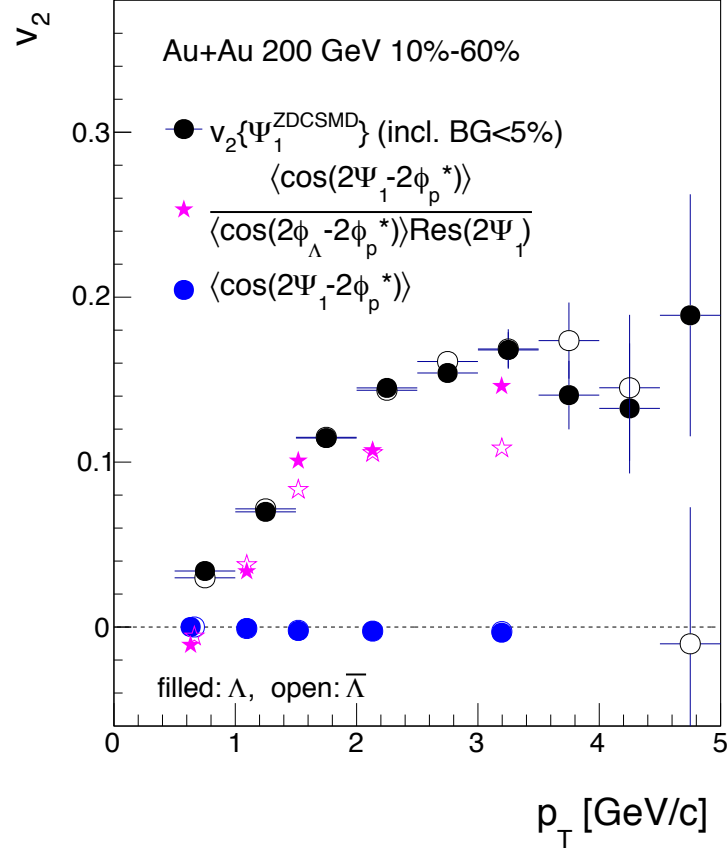


Fig. 63: v_2 measured with respect to the first-order event plane and estimated from the parameter p_2 in 10%-60% centrality bin.

References

- [1] B. I. Abelev *et al.* (STAR Collaboration), Phys. Rev. C **76**, 024915 (2007)
- [2] L. Adamczyk *et al.* (STAR Collaboration), arXiv:1701.06657
- [3] I. Karpenko and F. Becattini, Eur. Phys. J. C (2017) 77: 213
- [4] H. Li, L. Pang, Q. Wang, and X. Xia, arXiv:1704.01507 (2017)
- [5] T. Niida and S. Voloshin, STAR Analysis Note PSN0652, Charge-dependent directed flow in Cu+Au collisions at $\sqrt{s_{NN}} = 200$ GeV
- [6] T. Niida and S. Voloshin, STAR Analysis Note PSN0674, Systematic study of azimuthal anisotropy in Cu+Au collisions at $\sqrt{s_{NN}} = 200$ GeV
- [7] A. M. Poskanzer and S. A. Voloshin, Phys. Rev. C **58**, 1671 (1998)
- [8] F. Becattini, I. Karpenko, M. Lisa, I. Upsal, and S. Voloshin, Phys. Rev. C **95**, 054902 (2017)
- [9] M. M. Aggarwal *et al.* (STAR Collaboration), Phys. Rev. C **83**, 024901 (2011)
- [10] Y. Jiang, Z. Lin, and J. Liao, Phys. Rev. C **94**, 044910 (2016)
- [11] F. Becattini and Iu. Karpenko, arXiv:1707.07984; private communication
- [12] C. Patrignani *et al.* (Particle Data Group), Chin. Phys. C 40, 100001 (2016)
- [13] L. Adamczyk *et al.* (STAR Collaboration), Phys. Rev. Lett. **116**, 062301 (2016)
- [14] D. E. Kharzeev, J. Liao, S. A. Voloshin, and G. Wang, Prog. Part. Nucl. Phys. 88, 128 (2016)